Monthly Notices
of the
ROYAL ASTRONOMICAL SOCIETY

MNRAS **469,** 3141–3162 (2017)
Advance Access publication 2017 May 1

doi:10.1093/mnras/stx1048

Extreme jet ejections from the black hole X-ray binary V404 Cygni

A. J. Tetarenko,[1]★ G. R. Sivakoff,[1] J. C. A. Miller-Jones,[2] E. W. Rosolowsky,[1] G. Petitpas,[3] M. Gurwell,[3] J. Wouterloot,[4] R. Fender,[5] S. Heinz,[6] D. Maitra,[7] S. B. Markoff,[8] S. Migliari,[9,10] M. P. Rupen,[11,12] A. P. Rushton,[5,13] D. M. Russell,[14] T. D. Russell[8,2] and C. L. Sarazin[15]

[1]*Department of Physics, University of Alberta, CCIS 4-181, Edmonton, AB T6G 2E1, Canada*
[2]*International Centre for Radio Astronomy Research, Curtin University, GPO Box U1987, Perth, WA 6845, Australia*
[3]*Harvard-Smithsonian Center for Astrophysics, Cambridge, MA 02138, UK*
[4]*East Asian Observatory, 660 North Aohoku Place, University Park, Hilo, HI 96720, USA*
[5]*Department of Physics, Astrophysics, University of Oxford, Keble Road, Oxford OX1 3RH, UK*
[6]*Astronomy Department, University of Wisconsin-Madison, 475. N. Charter St., Madison, WI 53706, USA*
[7]*Department of Physics and Astronomy, Wheaton College, Norton, MA 02766, USA*
[8]*Anton Pannekoek Institute for Astronomy, University of Amsterdam, PO Box 94249, NL-1090 GE Amsterdam, the Netherlands*
[9]*Department of Astronomy and Meteorology, University of Barcelona, Martí i Franquès 1, E-08028 Barcelona, Spain*
[10]*XMM-Newton Science Operations Centre, ESAC/ESA, PO Box 78, E-28691 Villanueva de la Cañada, Madrid, Spain*
[11]*National Research Council, Herzberg Astronomy and Astrophysics, 717 White Lake Road, PO Box 248, Penticton, BC V2A 6J9, Canada*
[12]*National Radio Astronomy Observatory, PO Box 0, Socorro, NM 87801, USA*
[13]*School of Physics and Astronomy, University of Southampton, Highfield, Southampton SO17 1BJ, UK*
[14]*New York University Abu Dhabi, PO Box 129188, Abu Dhabi, United Arab Emirates*
[15]*Department of Astronomy, University of Virginia, PO Box 400325, Charlottesville, VA 22904, USA*

Accepted 2017 April 27. Received 2017 April 27; in original form 2017 March 20

ABSTRACT

We present simultaneous radio through sub-mm observations of the black hole X-ray binary (BHXB) V404 Cygni during the most active phase of its June 2015 outburst. Our 4 h long set of overlapping observations with the Very Large Array, the Sub-millimeter Array and the James Clerk Maxwell Telescope (SCUBA-2) covers eight different frequency bands (including the first detection of a BHXB jet at 666 GHz/450 μm), providing an unprecedented multifrequency view of the extraordinary flaring activity seen during this period of the outburst. In particular, we detect multiple rapidly evolving flares, which reach Jy-level fluxes across all of our frequency bands. With this rich data set, we performed detailed MCMC modelling of the repeated flaring events. Our custom model adapts the van der Laan synchrotron bubble model to include twin bi-polar ejections, propagating away from the black hole at bulk relativistic velocities, along a jet axis that is inclined to the line of sight. The emission predicted by our model accounts for projection effects, relativistic beaming and the geometric time delay between the approaching and receding ejecta in each ejection event. We find that a total of eight bi-polar, discrete jet ejection events can reproduce the emission that we observe in all of our frequency bands remarkably well. With our best-fitting model, we provide detailed probes of jet speed, structure, energetics and geometry. Our analysis demonstrates the paramount importance of the mm/sub-mm bands, which offer a unique, more detailed view of the jet than can be provided by radio frequencies alone.

Key words: black hole physics – stars: individual: V404 Cygni, GS 2023+338 – ISM: jets and outflows – radio continuum: stars – submillimetre: stars – X-rays: binaries.

1 INTRODUCTION

Black hole X-ray binaries (BHXBs), the rapidly evolving, stellar-mass counterparts of active galactic nuclei, are ideal candidates with which to study accretion and accretion-fed outflows, such as relativistic jets. These transient binary systems, containing a black

★E-mail: tetarenk@ualberta.ca

hole accreting mass from a companion star, occasionally enter into bright outburst phases lasting days to weeks, providing a real time view of the evolving relativistic jets (probed by radio through IR frequencies) and accretion flow (probed at X-ray frequencies).

BHXBs display two different types of relativistic jets, dependent on the mass accretion rate in the system (Fender, Belloni & Gallo 2004). At lower mass accretion rates ($<10^{-1}L_{\rm Edd}$),[1] during the hard accretion state (see Remillard & McClintock 2006 and Belloni 2010 for a review of accretion states in BHXBs), a steady, compact synchrotron-emitting jet is believed to be present in all BHXBs. It has also been shown that the compact jet is not only present during outburst phases, but can persist down into quiescence, at $<10^{-5}L_{\rm Edd}$ (Gallo, Fender & Hynes 2005; Plotkin, Gallo & Jonker 2013; Plotkin et al. 2015, 2016). At higher mass accretion rates, during the transition between accretion states, discrete jet ejecta are launched (e.g. Mirabel & Rodríguez 1994; Hjellming & Rupen 1995; Corbel et al. 2002; Miller-Jones et al. 2012a), and the compact jet may become quenched (Fender et al. 1999d; Corbel et al. 2001; Coriat et al. 2011; Russell et al. 2011; Rushton et al. 2016). A small number of BHXBs have been observed to display multiple jet ejection events within a single outburst (e.g. Mirabel & Rodríguez 1994; Hjellming & Rupen 1995; Tingay et al. 1995; Fender et al. 1999a; Kuulkers et al. 1999; Brocksopp et al. 2002, 2013).

Compact jets are characterized by a flat to slightly inverted optically thick spectrum ($\alpha > 0$; where $f_\nu \propto \nu^\alpha$; Fender 2001), extending from radio up to sub-mm or even infrared frequencies (Corbel & Fender 2002; Casella et al. 2010; Tetarenko et al. 2015a). Around infrared frequencies the jet emission becomes optically thin ($\alpha \sim -0.7$; Russell et al. 2013a), resulting in a spectral break. Each frequency below this break probes emission (from the optical depth, $\tau = 1$ surface) coming from a narrow range of distances downstream in the jet, where higher frequencies originate from regions along the jet axis that are closer to where the jet is launched (Blandford & Königl 1979; Falcke & Biermann 1995). The exact spectral shape (i.e. spectral index, location of the spectral break) is believed to evolve with changing jet properties such as geometry, magnetic field structure, and particle density profiles (Heinz & Sunyaev 2003; Markoff, Nowak & Wilms 2005; Casella & Pe'er 2009; Russell et al. 2013b; van der Horst et al. 2013; Russell et al. 2014), as well as the plasma conditions in the region where the jet is first accelerated (Polko, Meier & Markoff 2010, 2013, 2014; Koljonen et al. 2015).

In contrast to the compact jets, jet ejecta are characterized by an optically thin spectrum ($\alpha < 0$), give rise to bright flaring activity and can be routinely resolved with very long baseline interferometry (VLBI; e.g. Fender 2006). The accompanying flares typically have well-defined rise and decay phases, where the flares are usually optically thick in the rise phase, until the self-absorption turnover in the spectrum has passed through the observing band. These jet ejection events are believed to be the result of the injection of energy and particles to create an adiabatically expanding synchrotron-emitting plasma, threaded by a magnetic field (i.e. van der Laan synchrotron bubble model, hereafter referred to as the vdL model; van der Laan 1966; Hjellming & Johnson 1988; Hjellming & Han 1995). In this model, as the source expands the evolving optical depth results in the distinct observational signature of the lower frequency emission being a smoothed, delayed version of the higher frequency emission. The ejection events have been linked to both X-ray spectral and timing signatures (e.g. Fender, Homan & Belloni 2009; Miller-Jones et al. 2012a; Russell et al. 2014; Kalemci et al. 2016), although a definitive mechanism or sequence of events leading to jet ejection has not yet been identified.

Additionally, an extremely rare jet phenomenon, so called jet oscillation events, has also been observed in two BHXBs, GRS 1915+105 (radio, mm, IR; Pooley & Fender 1997) and V4641 Sgr (optical band; Uemura et al. 2004). Such rare events seem to occur only when the accretion rate is at very high fractions of the Eddington rate. These quasi-periodic oscillations (see Fender & Belloni 2004 for a review) show lower frequency emission peaking at later times (consistent with the vdL model for expanding discrete jet ejecta), rise and decay times of the repeated flares that are similar at all frequencies, and time lags between frequencies that vary within a factor of two. Moreover, no discrete moving components were resolved with VLBI during these oscillation events (although we note this could very well be due to sensitivity limits or the difficulty of synthesis imaging of fast-moving, time-variable components). As such, the exact nature of these events remains unclear, with theories including discrete plasma ejections, internal shocks in a steady flow or variations in the jet power in a self-absorbed, conical outflow (e.g. Fender & Pooley 1998, 2000; Collins, Kaiser & Cox 2003). In GRS 1915+105, these oscillations have also been clearly associated with dips in hard X-ray emission, possibly linking the launching of jet ejecta to the ejection and refilling of the inner accretion disc or coronal flow (Belloni et al. 1997; Mirabel et al. 1998; Vadawale et al. 2001).

While several transient BHXBs may undergo an outburst period in a given year, in which the jet emission becomes bright enough for detailed multiwavelength studies, only rare (e.g. once per decade) outbursts probe the process of accretion and the physics of accretion-fed outflows near (or above) the Eddington limit. Observing the brightest and most extreme phases of accretion during these outbursts presents us with a unique opportunity to study jet and accretion physics in unprecedented detail. On 2015 June 15, the BHXB V404 Cygni entered into one of these rare near-Eddington outbursts. In this paper, we report on our simultaneous radio through sub-mm observations of V404 Cygni during the most active phase of this outburst.

1.1 V404 Cygni

V404 Cygni (aka GS 2023+338; hereafter referred to as V404 Cyg) is a well-studied BHXB that has been in a low-luminosity quiescent state since its discovery with the *Ginga* satellite in 1989 (Makino 1989). This source has been observed to undergo a total of three outbursts prior to 2015; most recently in 1989 (Han & Hjellming 1992; Terada et al. 1994; Oosterbroek et al. 1997), and two prior to 1989 which were recorded on photographic plates (Richter 1989). V404 Cyg is known to display bright X-ray luminosities and high levels of multiwavelength variability, both in outburst and quiescence (Hjellming & Han 1989; Kitamoto et al. 1989; Tanaka & Lewin 1995; Hynes, Zurita & Haswell 2002). The prolonged quiescent period of V404 Cyg, and high quiescent luminosity ($L_{\rm X} \sim 1 \times 10^{33}\,{\rm erg\,s^{-1}}$; Corbel, Kording & Kaaret 2008), has allowed the complete characterization of the system. The optical extinction is low, with $E(B-V) = 1.3$, enabling the study of the optical counterpart, and the determination of the mass function as $6.08 \pm 0.06\,{\rm M}_\odot$ (Casares, Charles & Naylor 1992; Casares &

[1] The Eddington luminosity is the theoretical limit where, assuming ionized hydrogen in a spherical geometry, radiation pressure balances gravity. This limit corresponds to $L_{\rm Edd} = 1.26 \times 10^{38} M/{\rm M}_\odot\,{\rm erg\,s^{-1}}$, where M is the black hole mass.

Charles 1994). Subsequent modelling determined the black hole mass to be $9.0^{+0.2}_{-0.6}\,M_{\odot}$, with an inclination angle of $67^{\circ}{}^{+3}_{-1}$, and an orbital period of 6.5 d (Shahbaz et al. 1994; Khargharia, Froning & Robinson 2010). However, we note that this inclination angle estimate is dependent on the assumed level of accretion disc contamination in the optical light curves being modelled. Khargharia et al. (2010) assumed <3 per cent accretion disc contamination, but given that V404 Cyg is known to be variable in quiescence in the optical, it is plausible that the accretion disc contamination may be larger (Zurita, Casares & Shahbaz 2003; Bernardini et al. 2016a), which would imply a larger inclination angle. Further, the faint, unresolved radio emission from the quiescent jets was used to determine a model-independent parallax distance of 2.39 ± 0.14 kpc (Miller-Jones et al. 2009b), making V404 Cyg one of the closest known BHXBs in the Galaxy. The close proximity, well-determined system parameters and bright multiwavelength activity make this system an ideal target for jet and accretion studies.

On 2015 June 15,[2] V404 Cyg entered into its fourth recorded outburst period. The source began exhibiting bright multiwavelength flaring activity (e.g. Ferrigno et al. 2015a; Gandhi et al. 2015; Gazeas et al. 2015; Mooley et al. 2015; Motta et al. 2015a,b; Tetarenko et al. 2015b,c) immediately following the initial detection of the outburst in X-rays (Barthelmy et al. 2015; Kuulkers et al. 2015; Negoro et al. 2015), and swiftly became the brightest BHXB outburst seen in the past decade. This flaring behaviour was strikingly similar to that seen in the previous 1989 outburst (Terada et al. 1994; Oosterbroek et al. 1997; Zycki, Done & Smith 1999). Towards the end of June, the flaring activity began to diminish across all wavelengths (e.g. Ferrigno et al. 2015b; Martin-Carrillo et al. 2015; Oates et al. 2015; Scarpaci et al. 2015; Tetarenko et al. 2015d; Tsubono et al. 2015), and the source began to decay (Sivakoff et al. 2015a,b), reaching X-ray quiescence[3] in early to mid-August (Sivakoff et al. 2015c; Plotkin et al. 2017). V404 Cyg also showed a short period of renewed activity from late December 2015 to early January 2016 (e.g. Beardmore, Page & Kuulkers 2015; Lipunov et al. 2015; Malyshev et al. 2015; Trushkin, Nizhelskij & Tsybulev 2015; Motta et al. 2016; Tetarenko et al. 2016), and Munoz-Darias et al. (2017) present radio, optical and X-ray monitoring during this period.

We organized simultaneous observations with the Karl G. Jansky Very Large Array (VLA), the Sub-millimeter Array (SMA) and the James Clerk Maxwell Telescope (JCMT) on 2015 June 22 (approximately 1 week following the initial detection of the outburst), during which time some of the brightest flaring activity seen in the entire outburst was observed. This comprehensive data set gives us an unprecedented multifrequency view of V404 Cyg, in turn allowing us to perform detailed multifrequency light-curve modelling of the flaring events. In Section 2, we describe the data collection and data reduction processes. Section 3 describes the custom procedures our team developed to extract high time resolution measurements from our data. In Section 4, we present our multifrequency light curves, outline our model and describe the modelling process. A discussion of our best-fitting model is presented in Section 5, and a summary of our work is presented in Section 6.

[2] Bernardini et al. (2016a) serendipitously detected an optical precursor to this outburst on June 8/9, approximately 1 week prior to the first X-ray detection.

[3] V404 Cyg entered optical quiescence in mid-October 2015 (Bernardini, Russell & Lewis 2016b).

2 OBSERVATIONS AND DATA ANALYSIS

2.1 VLA radio observations

We observed V404 Cyg with the VLA (Project Code: 15A-504) on 2015 June 22, with scans on source from 10:37:24 to 14:38:39 UTC (MJD = 57195.442–57195.610) in both C (4–8 GHz) and K (18–26 GHz) band. The array was in its most extended A configuration, where we split the array into two sub-arrays of 14 (sub-array A) and 13 (sub-array B) antennas. Sub-array A observed the sequence C-K-C, while sub-array B observed the sequence K-C-K, with an 80 s on target and 40 s on calibrator cycle, in order to obtain truly simultaneous observations across both bands. All observations were made with an 8-bit sampler, comprised of two base-bands, with eight spectral windows of sixty-four 2 MHz channels each, giving a total bandwidth of 1.024 GHz per base-band. Flagging, calibration and imaging of the data were carried out within the Common Astronomy Software Application package (CASA; McMullin et al. 2007) using standard procedures. We used 3C48 (0137+331) as a flux calibrator and J2025+3343 as a phase calibrator for both sub-arrays. No self-calibration was performed. Due to the rapidly changing flux density of the source, we imaged the source (with natural weighting; see the Appendix for details on our choice of weighting scheme) on time-scales as short as the correlator dump time (2 s) using our custom CASA timing scripts (see Section 3.1 for details).

2.2 SMA (Sub)-millimetre observations

We observed V404 Cyg with the SMA (Project Code: 2015A-S026) on 2015 June 22, with scans on source from 10:16:17 to 18:20:47 UTC (MJD = 57195.428–57195.764), and the correlator tuned to an LO frequency of 224 GHz. The array was in the sub-compact configuration with a total of seven antennas (out of a possible eight antennas). These observations were made with both the Application Specific Integrated Circuit (ASIC) and SMA Wideband Astronomical ROACH2 Machine (SWARM) (Primiani et al. 2016) correlators active, to yield two side-bands, with 48 spectral windows of one hundred twenty-eight 0.8125 MHz channels (ASIC) and an additional two 1.664 GHz spectral windows (SWARM), giving a total bandwidth of 8.32 GHz per side-band. The SWARM correlator had a fixed resolution of 101.6 kHz per channel, and thus originally 16 383 channels for each SWARM spectral window. Given the continuum nature of these observations, we performed spectral averaging, to yield 128 13 MHz channels in both SWARM spectral windows, to match the number of channels in the ASIC spectral windows, and in turn make it easier to combine ASIC and SWARM data. We used 3C454.3 (J2253+1608) as a bandpass calibrator, MWC349a and J2015+3710 as phase calibrators, and Neptune and Titan as flux calibrators.[4] We note that only the second IF (spectral windows 25–50) was used for flux calibration in the upper side-band due to a CO line that was present in both flux calibrators at 230.55 GHz. Our observing sequence consisted of a cycle of 15 min on target and 2.5 min on each of the two phase calibrators. As CASA is unable to handle SMA data in its original format, prior to any data reduction we used the SMA scripts, sma2casa.py and smaImportFix.py, to convert the data into CASA MS format, perform the T_{sys} corrections, and spectrally average the two SWARM spectral windows. Flagging, calibration and imaging of the data were then performed in CASA using procedures outlined in the CASA Guides for SMA data

[4] The SMA calibrator list can be found at http://sma1.sma.hawaii.edu/callist/callist.html

reduction.[5] Due to the rapidly changing flux density of the source, we imaged the source (with natural weighting; see the Appendix for details on our choice of weighting scheme) on time-scales as short as the correlator dump time (30 s) using our custom CASA timing scripts (see Section 3.1 for details).

2.3 JCMT SCUBA-2 (sub)-millimetre observations

We observed V404 Cyg with the JCMT (Project Code: M15AI54) on 2015 June 22 from 10:49:33 to 15:12:40 UTC (MJD = 57195.451–57195.634), in the 850 μm (350 GHz) and 450 μm (666 GHz) bands. The observation consisted of eight ∼30 min scans on target with the SCUBA-2 detector (Chapin et al. 2013; Holland et al. 2013). To perform absolute flux calibration, observations of the calibrator CRL2688 were used to derive a flux conversion factor (Dempsey et al. 2012). The daisy configuration was used to produce 3 arcmin maps of the target source region. During the observations, we were in the Grade 3 weather band with a 225 GHz opacity of 0.095–0.11. Data were reduced in the Starlink package using both standard procedures outlined in the SCUBA-2 cookbook[6] and SCUBA-2 Quickguide,[7] as well as a custom procedure to create short time-scale maps (time-scales shorter than the 30 min scan time-scale) to extract high time resolution flux density measurements of the rapidly evolving source (see Section 3.2 for details).

3 HIGH TIME RESOLUTION MEASUREMENTS

3.1 VLA and SMA

To obtain high time resolution flux density measurements of V404 Cyg from our interferometric data sets (VLA and SMA), we developed a series of custom scripts that run within CASA. A detailed account of the development and use of these scripts will be presented in Tetarenko et al. (in preparation), although we provide a brief overview of the capabilities here.

Our scripts split an input calibrated CASA measurement set into specified time intervals for analysis in the image plane or the uv plane. In the image plane analysis, each time interval is cleaned and the flux density of the target source is measured by fitting a point source in the image plane with the native CASA task `imfit`. All imaging parameters (e.g. image size, pixel size, number of CLEAN iterations, CLEAN threshold) can be fully specified. In the uv plane analysis, the UVMULTFIT package (Marti-Vidal et al. 2014) is used to measure flux density of the target source. In either case, an output data file and plot of the resulting light curve are produced. These scripts are publicly available on github,[8] and are being implemented as a part of an interactive service our team is developing to run on Amazon Web Services Cloud Resources.

All VLA and SMA flux density measurements output from this procedure (fitting only in the image plane) are provided in a machine readable table online, which accompanies this paper. Additionally, to check that the variability we observed in V404 Cyg is dominated by intrinsic variations in the source and not due to atmospheric or instrumental effects, we also ran our calibrator sources through these scripts (see the Appendix for details).

3.2 JCMT SCUBA-2

To obtain high time resolution flux density measurements of V404 Cyg from our JCMT SCUBA-2 data, we developed a custom procedure to produce a data cube, containing multiple maps of the target source region, at different time intervals throughout our observation.

We run the Starlink Dynamic Iterative Mapmaker tool on each of the target scans, using the bright compact recipe, with the addition of the shortmap parameter. The shortmap parameter allows the Mapmaker to create a series of maps, each of which will include data from a group of adjacent time slices. The number of time slices included in each map is equivalent to the shortmap parameter value. At 850 μm, we use shortmap = 200 to produce 362 time slices for a 32 min scan, resulting in 5 s time bins. At 450 μm shortmap = 400 would produce the same number of time slices, where a factor of 2 is applied as the default pixel size is 2 arcsec at 450 μm and 4 arcsec at 850 μm. However, as the noise is higher at 450 μm, we use shortmap = 4800 to produce 32 time slices for a 32 min scan, resulting in 60 s time bins. The `stackframes` task is then used to combine all of the short maps into a cube for each scan. The sort = True and sortby = MJD-AVG parameters ensure the maps are ordered chronologically in time, with the resulting cube having the dimensions, position X (pixels), position Y (pixels), time (MJD). Using the `wcsmosaic` task, we then combined the cubes from all the scans. We calibrated the combined cube into units of Jy using the `scuba2checkcal` and `cmult` tasks. Finally, the combined cube can be viewed in *Gaia*, and converted to FITS format with the `ndf2fits` task.

To extract flux densities from each time slice in the combined cube, we fit a 2D Gaussian[9] with the size of the beam (FWHM of 15.35 arcsec at 850 μm and 10.21 arcsec at 450 μm; derived using the task `scuba2checkcal`) to each slice of the cube. All JCMT SCUBA-2 flux density measurements output from this procedure are provided in a machine readable table online, which accompanies this paper. As with our interferometric data sets, to check that the variability we observed in V404 Cyg is dominated by intrinsic variations in the source and not due to atmospheric or instrumental effects, we also ran this procedure on our calibrator source scans (see the Appendix for details).

4 RESULTS

4.1 Multifrequency light curves

A composite light curve of all of our VLA, SMA and JCMT observations from June 22 is presented in Fig. 1. We observe rapid multifrequency variability in the form of multiple large-scale flares, reaching Jy flux levels. In the SMA data, the largest flare (at ∼13:15 UTC) rose from ∼100 mJy to a peak of ∼5.6 Jy on a time-scale of ∼25 min. The JCMT SCUBA-2 data appear to track the SMA data closely, with the largest flare at 350 GHz rising from ∼400 mJy to a peak of ∼7.2 Jy on a time-scale of ∼18 min. This is the largest mm/sub-mm flare ever observed from a BHXB, far surpassing even the brightest events in GRS 1915+105 (Fender & Pooley 2000). The VLA radio data lag the mm/sub-mm (where

[5] Links to the SMA CASA Guides and these scripts are publicly available at https://www.cfa.harvard.edu/sma/casa

[6] http://starlink.eao.hawaii.edu/devdocs/sc21.htx/sc21.html

[7] https://www.eaobservatory.org/jcmt/instrumentation/continuum/scuba-2/data-reduction/reducing-scuba2-data

[8] https://github.com/Astroua/AstroCompute_Scripts

[9] The PYTHON package GAUSSFITTER is used in the Gaussian fitting; https://github.com/keflavich/gaussfitter

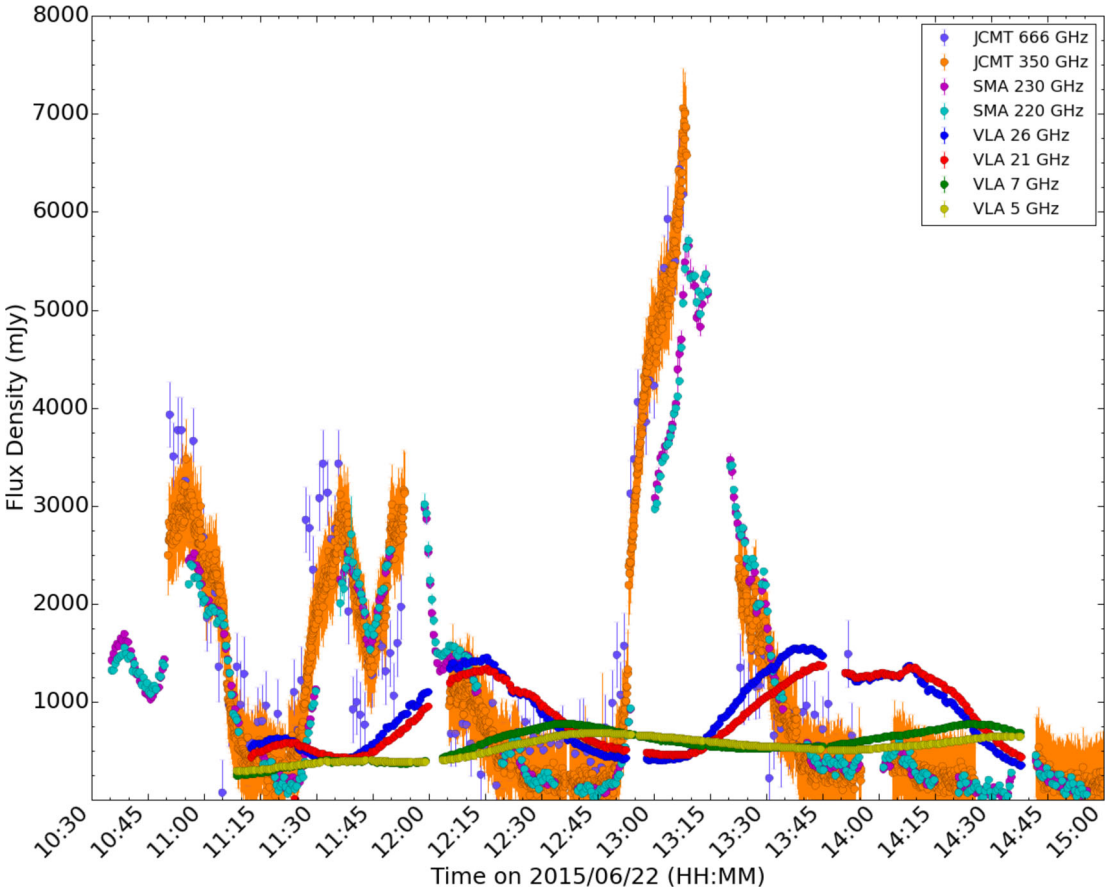

Figure 1. Simultaneous radio through sub-mm light curves of the BHXB V404 Cygni during the most active phase of its June 2015 outburst. These light curves sample the brightest flares at these frequencies over the entire outburst. All light curves are sampled at the finest time resolution possible, limited only by the correlator dump time (and the sensitivity for JCMT data). The VLA light curves have 2 s time bins, the SMA light curves have 30 s time bins, the JCMT SCUBA-2 350 GHz (850 μm) light curve has 5 s time bins and the JCMT SCUBA-2 666 GHz (450 μm) light curve has 60 s time bins. The mm/sub-mm regime samples a much more extreme view of the flaring activity than the radio regime, with detailed sub-structure detected only in the mm/sub-mm light curves.

the lag appears to be variable among the flares; ∼20–45 min and ∼40–75 min between 350 GHz and the 18–26 GHz and 4–8 GHz bands, respectively), with flares in the 18–26 GHz band rising to a peak of ∼1.5 Jy on a time-scale of ∼35 min, and flares in the 4–8 GHz band rising to a peak of ∼780 mJy on a time-scale of ∼45 min.

Upon comparing the multifrequency emission, it is clear that the mm/sub-mm data provide a much more extreme view of the flaring activity than the radio emission. In particular, there is more structure present in the mm/sub-mm light curves when compared to the radio light curves. As such, while not immediately apparent in the radio light curves, the mm/sub-mm data suggest that each of the three main flares in the light curves is actually the result of the superposition of emission from multiple flaring components. Additionally, the lower frequency emission in the light curves appears to be a smoothed, delayed version of the high-frequency emission (with the flares showing longer rise times at lower frequencies). This emission pattern is consistent with an expanding outflow structure, where the mm/sub-mm emission originates in a region (with a smaller cross-section) closer to the black hole, and has thus not been smoothed out to as high a degree as the radio emission, as the material expands and propagates outwards. Therefore, all of these observations suggest that the emission in our light curves could be dominated by emission from multiple, expanding, discrete jet ejection events (van der Laan 1966).

Further, we notice that the baseline flux level at which the flaring begins at each frequency in our light curves appears to vary. This suggests that there is an additional frequency-dependent component contributing to our light curves, on top of the discrete jet ejecta. In an effort to determine the origin of this extra emission, assuming that the baseline emission is constant in time, we create a spectrum of this emission by estimating the baseline flux level at each frequency (we performed iterative sigma clipping and take the minimum of the resulting sigma clipped data). This spectrum[10] is presented in Fig. 2, where it appears as though the baseline emission could be described by a broken power law or a single power law (with higher frequency emission displaying a lower baseline level than lower frequency emission). This spectral shape, combined with the fact that we observe a strong compact core component (in addition to resolved ejecta components) within simultaneous high-resolution radio imaging (Miller-Jones et al., in preparation), suggests that the baseline emission originates from an underlying compact jet that was not fully quenched.

[10] We note that these are only empirical initial estimates of the baseline flux at each frequency, and do not necessarily represent the flux of the compact jet in our model presented in Section 4.2.

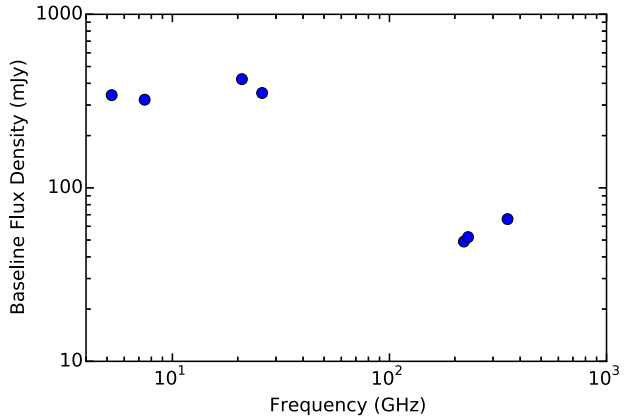

Figure 2. Estimated radio through sub-mm spectrum of the baseline flux component seen in our light curves.

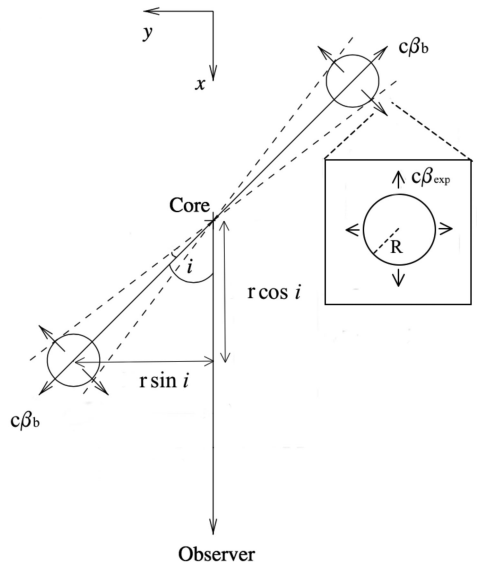

Figure 3. Schematic of the geometry for our jet model in a plane defined by our line of sight and the central axis of the jets (i.e. bird's eye view). The inset panel displays the ejecta component seen from the source frame (at rest with respect to the ejecta). All parameters are defined within the accompanying text. This figure was adapted from its original form in Miller-Jones, Fender & Nakar (2006).

4.2 V404 Cyg jet model

Given the morphology of our light curves outlined in the previous section, we have constructed a jet model for V404 Cyg that is capable of reproducing emission from multiple, repeated, discrete jet ejection events, on top of an underlying compact jet component. We define two coordinate frames, the observer frame and the source frame (at rest with respect to the ejecta components). We will compute our model primarily in the source frames, and then transform back to the observer frame. All variables with the subscript *obs* are defined in the observer frame. Schematics displaying the geometry of our model from different viewpoints are displayed in Figs 3 and 4.

In our model, the underlying compact jet is characterized by a broken power-law spectrum, where the flux density is independent

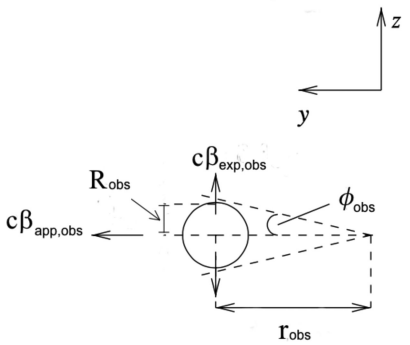

Figure 4. Schematic of the geometry of the discrete jet ejections in our model, as seen by the observer. All parameters are defined within the accompanying text. This figure was adapted from its original form in Miller-Jones et al. (2006).

of time and varies only with frequency according to,

$$F_{\nu,\mathrm{cj}} = \begin{cases} F_{\mathrm{br,cj}}(\nu/\nu_{\mathrm{br}})^{\alpha_1}, & \nu < \nu_{\mathrm{br}} \\ F_{\mathrm{br,cj}}(\nu/\nu_{\mathrm{br}})^{\alpha_2}, & \nu > \nu_{\mathrm{br}} \end{cases}. \quad (1)$$

Here, ν_{br} represents the frequency of the spectral break, $F_{\mathrm{br,\,cj}}$ represents the amplitude of the compact jet at the spectral break frequency, α_1 represents the spectral index at frequencies below the break and α_2 represents the spectral index at frequencies above the break. In the case where the spectral break frequency is located below the lowest sampled frequency band, or above the highest sampled frequency band, the underlying compact jet can be characterized by a single power-law spectrum, where $F_{\nu,\mathrm{cj}} = F_{0,\mathrm{cj}}\left(\frac{\nu}{\nu_0}\right)^{\alpha}$. Here, $F_{0,\,\mathrm{cj}}$ represents the amplitude of the compact jet at ν_0, and α represents the spectral index.

On top of the compact jet, we define a discrete ejection event as the simultaneous launching of two identical, bi-polar plasma clouds (an approaching and receding component). Each of these clouds evolves according to the vdL model (van der Laan 1966). In this model, a population of relativistic electrons, with a power-law energy distribution ($N(E)\,\mathrm{d}E = KE^{-p}\,\mathrm{d}E$), is injected into a spherical cloud threaded by a magnetic field. The cloud is then allowed to expand adiabatically, while the electrons and magnetic field are assumed to be kept in equipartition. As a result of the expansion, this model predicts the flux density of each cloud will scale as,

$$F_{\nu,\mathrm{ej}} = F_0\left(\frac{\nu}{\nu_0}\right)^{5/2}\left(\frac{R}{R_0}\right)^{3}\frac{1-\exp(-\tau_\nu)}{1-\exp(-\tau_0)}. \quad (2)$$

Here, R indicates the time-dependent radius of the cloud, and the synchrotron optical depth, τ_ν, at a frequency, ν, scales as,

$$\tau_\nu = \tau_0\left(\frac{\nu}{\nu_0}\right)^{-(p+4)/2}\left(\frac{R}{R_0}\right)^{-(2p+3)}. \quad (3)$$

Note that the subscript 0 in all our equations indicates values at the reference frequency,[11] at the time (or radius) of the peak flux of the component.

Taking the derivative of equation (2) with respect to time[12] (or radius), allows us to relate the optical depth at which the flux density

[11] We defined our reference frequency as the upper sideband in our SMA data (230 GHz).

[12] Our expression in equation (4) differs from that of van der Laan (1966), as he takes the derivative with respect to ν instead of time, yielding $\mathrm{e}^{\tau_0} - ([p+4]/5)\tau_0 - 1 = 0$.

of the reference frequency reaches a maximum, τ_0, to the power-law index of the electron energy distribution, p,

$$e^{\tau_0} - (2p/3 + 1)\tau_0 - 1 = 0. \quad (4)$$

Equation (4) has no analytic solution and thus must be solved numerically. Therefore, we choose to leave our model in terms of τ_0, and solve for p after the fitting process.

To describe the time-dependence of the cloud radius, a linear expansion model is used, according to,

$$R = R_0 + \beta_{\rm exp} c\,(t - t_0)\,. \quad (5)$$

Here, $\beta_{\rm exp}c$ represents the expansion velocity of the cloud, while R_0 can be expressed in terms of the distance to the source, d, peak flux, F_0, and optical depth, τ_0, of the cloud at the reference frequency (Yusef-Zadeh et al. 2008),

$$R_0 = \left[\frac{F_0 d^2}{\pi}\frac{1}{1-\exp(-\tau_0)}\right]^{1/2}. \quad (6)$$

At the same time that the clouds are expanding, they are also propagating away from the black hole at bulk relativistic velocities, along a jet axis that is inclined to the observer's line of sight (see Fig. 3). As such, the emission we observe will have been affected by projection effects, relativistic beaming and a geometric time delay between the approaching and receding clouds in each ejection event.

To account for these effects, we first assume that the clouds are travelling at a constant bulk velocity, $\beta_{\rm b}c$, and that the jet has a conical geometry (with an observed opening angle, $\phi_{\rm obs}$). In turn, the apparent observed velocity across the sky (derived via the transverse Doppler effect) is represented as (Mirabel & Rodríguez 1999),

$$\beta_{\rm app,obs} = \begin{cases} \dfrac{r\sin i}{c\,(t - t_{\rm ej}) - r\cos i} & \rightarrow \text{approaching,} \\ \dfrac{r\sin i}{c\,(t - t_{\rm ej}) + r\cos i} & \rightarrow \text{receding} \end{cases} \quad (7)$$

where $r = \beta_{\rm b}c(t - t_{\rm ej})$ is the distance travelled by the cloud away from the black hole, $t_{\rm ej}$ represents the ejection time, c represents the speed of light and i represents the inclination angle of the jet axis to the line of sight.

Equation (7) can be simplified by substituting in our expression for r to yield,

$$\beta_{\rm app,obs} = \beta_b \Gamma \delta_{\mp} \sin(i), \quad (8)$$

where the Doppler factor and bulk Lorentz factor are given by $\delta_{\mp} = \Gamma^{-1}[1 \mp \beta_{\rm b}\cos i]^{-1}$ and $\Gamma = (1 - \beta_{\rm b}^2)^{-1/2}$, respectively. The sign convention in the Doppler factor indicates that a δ_- should be used for the approaching cloud and a δ_+ should be used for the receding cloud.

From Figs 3 and 4,

$$\tan\phi_{\rm obs} = \frac{R_{\rm obs}}{r_{\rm obs}} = \frac{\delta_{\mp}\,\beta_{\rm exp}\,c\,(t - t_{ej})_{\rm obs}}{\beta_{\rm app,obs}\,c\,(t - t_{\rm ej})_{\rm obs}} = \frac{\delta_{\mp}\,\beta_{\rm exp}}{\beta_{\rm app,obs}}. \quad (9)$$

Combining equations (8) and (9), and solving for the bulk Lorentz factor, Γ, yields,

$$\Gamma = \left(1 + \frac{\beta_{\rm exp}^2}{\tan^2\phi_{\rm obs}\sin^2 i}\right)^{1/2}. \quad (10)$$

Rearranging equation (10) (and substituting in $1 - \Gamma^2 = -\Gamma^2\beta_{\rm b}^2$) gives the expansion velocity (to be input into equation 5) in terms of only the bulk velocity and jet geometry (inclination and opening angle), such that,

$$\beta_{\rm exp} = \tan\phi_{\rm obs}[\Gamma^2\{1 - (\beta_{\rm b}\cos i)^2\} - 1]^{1/2}. \quad (11)$$

Further, we wish to write our model in terms of only the ejection time ($t_{\rm ej}$), rather than the time of the peak flux at the reference frequency (t_0), without introducing any additional parameters. Using our definition that $R = R_0$ at the instant $t = t_0$, the two time-scales are related by,

$$t_0 = t_{\rm ej} + \frac{R_0}{\beta_{\rm exp}c}. \quad (12)$$

Lastly, we correct for relativistic beaming by applying a factor of $\delta_{\mp}^3$ (Longair 2011) to our flux density in equation (2), according to,

$$F_{\nu,\rm ej,obs} = \delta_{\mp}^3 F_{\nu,\rm ej}. \quad (13)$$

Here, $F_{\nu,\,\rm ej,\,obs}$ indicates the flux density of the cloud in the observer frame, at the observing frequency $\nu_{\rm obs}$, at the observed times since the zero-point of our observations, $\Delta t_{\rm obs}$, while $F_{\nu,\,\rm ej}$ indicates the flux density of the clouds in the source frame, at the frequency, $\nu = \delta_{\mp}^{-1}\nu_{\rm obs}$, at the times, $\Delta t = \delta_{\mp}\Delta t_{\rm obs}$.

All of the ejection events we model are not correlated, and thus evolve independently of each other. The total observed flux density in our model is represented as,

$$F_{\nu,\rm obs,tot} = \sum_i \delta_-^3 (F_{\nu,\rm i,app}) + \sum_i \delta_+^3 (F_{\nu,\rm i,rec}) + F_{\nu,\rm cj}. \quad (14)$$

4.2.1 *Jet precession*

In addition to our VLA, SMA and JCMT observations, we also obtained simultaneous high-angular resolution radio observations with the very long baseline array (VLBA). Through imaging the VLBA data set in short 2 min time bins, we resolve multiple discrete ejecta. Our analysis of these VLBA images has shown clear evidence of jet precession, where the position angle of the resolved ejecta change by up to 40° on an hourly time-scale (this result will be reported in detail in Miller-Jones et al., in preparation). As the emission predicted by our model is highly dependent on the inclination angle of the jet axis, we account for the effect of this rapid, large-scale jet precession in our model by allowing our inclination parameter, i, to vary between ejection events.

4.2.2 *Accelerated motion*

While we have assumed that the jet ejecta are travelling at constant bulk velocities, it is possible that they undergo some form of accelerated motion. To test this hypothesis, we generalized our model to allow the input of a custom bulk velocity profile, where we implemented simple velocity profiles to mimic a finite acceleration period where the cloud would approach a terminal velocity (e.g. a linear ramp function, a body subject to a quadratic drag force). However, in all cases, our best-fitting model either tended towards a constant velocity profile or would not converge. This result, while not ruling out the possibility of accelerated motion, suggests that any potential acceleration period may have only lasted for a short enough period of time that we are not able to discern the difference between the resulting light curves for the accelerated and constant bulk motion.

4.2.3 *Sub-conical jet geometry*

While we have assumed that the jet in our model is conical (constant opening angle), it is possible that the jet geometry could deviate from a strictly conical shape (especially on the au size scales we

Table 1. V404 Cyg jet model parameters and priors[a].

Parameter[b]	Description	Prior distribution[c]	Prior minimum	Prior maximum
$F_{0,\rm cj}$	Amplitude of compact jet component at ν_0 in mJy	Uniform	10	1000
α	Spectral index	Truncated normal ($\mu = -0.5, \sigma = 0.1$)	-1	0
$^*t_{\rm ej}$	Ejection time of bi-polar components in seconds[d,e]	Uniform	$t_g - 1000$	$t_g + 1000$
$^*i$	Inclination angle of the jet axis in degrees	Truncated normal ($\mu = 67, \sigma = 20$)	0	90
$^*\phi_{\rm obs}$	Observed opening angle in degrees	Uniform	1	20
$^*\tau_0$	Optical depth at the reference frequency	Truncated normal ($\mu = 2.0, \sigma = 0.3$)	1	3
$^*F_0$	Peak flux density at the reference frequency in mJy	Truncated normal ($\mu = 3000, \sigma = 1000$)	0	6000
$^*\beta_b$	Bulk jet speed in units of c	Inverse gamma ($a = 3$)[f]	0	1

[a]Note that the emission from the underlying compact jet portion of our model is best fitted by a single power law rather than a broken power law. Therefore, only the parameters describing the single power-law version of the compact jet in our model are shown here.
[b]Parameters marked with a * indicate those that are allowed to vary between ejection events.
[c]Justification of our use of these priors is presented in the text of Section 4.3.
[d]For simplicity, when modelling we convert our times to units of seconds past the zero-point of MJD 57195.41806.
[e]$t_{\rm g}$ represents the initial guess of the ejection time, see Section 4.3 for details.
[f]The inverse gamma distribution takes the form, $f(x) = \frac{x^{(-a-1)}}{\Gamma(a)} \exp(-1/x)$, where Γ represents the gamma function not the bulk Lorentz factor. This distribution is a common prior used for small number parameters defined to be <1.

are probing), where the opening angle (and in turn the expansion speed of the ejecta) could change with time. In particular, if we assume that the jet confinement mechanism is external, then the jet geometry will depend on the adiabatic indices of the two media (i.e. the jet and its surrounding medium). A relativistic plasmon confined by the internal pressure of a terminal spherical wind (made up of a $\Gamma = 5/3$ gas) will expand sub-conically, according to $R \propto r^{5/6}$. To test this scenario, we modified our model to use the above sub-conical expansion expression in place of equation (5). In doing this, we find that our best-fitting model still tend towards constant expansion speed/opening angle profiles for all the ejecta. This result, while not ruling out a non-conical jet geometry, could suggest that any deviations from a conical jet shape only occur on sub-au size scales, probing time-scales before the sub-mm emission peaks, and thus we are not able to discern the difference between the resulting light curves for conical/sub-conical jet geometry.

4.2.4 Bi-polar versus single-sided ejections

Our jet model assumes that each ejection event takes the form of two identical, oppositely directed plasmons. However, in principle our light curves could also be fitted with a collection of single-sided ejections. These unpaired components could occur as a result of Doppler boosting of highly relativistic plasmons causing us to observe only the approaching component of an ejecta pair, or intrinsically unpaired ejecta. Our simultaneous VLBA imaging may help distinguish between these two scenarios. We resolve both paired and (possibly[13]) unpaired ejecta components in our VLBA images, which could suggest that the emission in our light curves is produced by a combination of bi-polar and single-sided ejection events. Using these VLBA results to include stricter constraints within our model on ejecta numbers, type (single/bi-polar) and ejection times, is beyond the scope of this work, but will be considered in a future iteration of the model.

[13] Given the rapid time-scales of the ejections, multiple ejecta can become blended together in these images, making it difficult at times to conclusively identify and track individual components.

4.3 Modelling process and best-fitting model

Due to the large number of free parameters in our model, we use a Bayesian approach for parameter estimation. In particular, we apply a Markov-Chain Monte Carlo algorithm (MCMC), implemented with the EMCEE package (Foreman-Mackey et al. 2013), to fit our light curves with our jet model. This package is a pure-PYTHON implementation of Goodman & Weare's Affine Invariant MCMC Ensemble Sampler (Goodman & Weare 2010), running a modified version of the commonly used Metropolis-Hastings Algorithm, whereby it simultaneously evolves an ensemble of 'walkers' through the parameter space. We use 500 walkers (10 × the number of dimensions in our model) for our MCMC runs.

Prior distributions used for all of our parameters are listed in Table 1. We choose physically informative priors that reflect our knowledge of V404 Cyg (or commonly assumed values for BHXBs) where possible, and wide uninformative uniform priors when we have no pre-defined expectation for a specific parameter. For instance, the prior for the inclination angle is set as a truncated normal distribution, centred on 67° (the measured inclination angle of the system), with boundaries of 0° and 90° (allowed values of the inclination angle). On the other hand, the prior for the ejection time is simply a uniform distribution, sampling a wide range of possible times around our best initial guess.

Before running the MCMC, the initial position of the walkers in the parameter space needs to be defined. As the performance of the EMCEE algorithm tends to benefit heavily from well-defined initial conditions, we do an initial exploration of the parameter space using a harmony search global optimization algorithm.[14] This meta-heuristic algorithm, that is similar to, but much more efficient than a brute force grid search method (which would not be computationally feasible in this case), yields a reasonable initial guess for our model, and we place our walkers in a tight ball around this initial guess in the parameter space.

As our jet model can predict emission at multiple frequencies, to reduce the degeneracy in our model, we choose to simultaneously fit all of our multifrequency data sets, except for the JCMT 666 GHz data set, due to its sparser sampling and larger uncertainty in flux

[14] Implemented in the PYTHON package, PYHARMONYSEARCH; https://github.com/gfairchild/pyHarmonySearch

Table 2. V404 Cyg jet model best-fitting parameters.

Compact jet parameters[a]										
$F_{0,\rm cj}$ (mJy)	α									
$56.22^{+0.19}_{-0.21}$	$-0.46^{+0.03}_{-0.03}$									
Individual jet ejecta parameters										
Ejection	$t_{\rm ej}$ (HH:MM:SS.S)	$t_{\rm ej}$ (MJD)	i (°)	$\phi_{\rm obs}$ (°)	τ_0	p^b	F_0 (mJy)	$\beta_{\rm b}$ (v/c)	$\beta_{\rm exp}$ (v/c)[c]
1	$10{:}23{:}42.4^{+8.5}_{-8.0}$	$57195.4331^{+0.0001}_{-0.0001}$	$39.73^{+1.64}_{-1.57}$	$4.06^{+0.24}_{-0.22}$	$1.96^{+0.01}_{-0.01}$	$3.18^{+0.03}_{-0.03}$	$986.8^{+6.2}_{-5.4}$	$0.290^{+0.006}_{-0.006}$	$0.014^{+0.001}_{-0.001}$
2	$10{:}36{:}09.4^{+3.6}_{-3.4}$	$57195.4418^{+0.0001}_{-0.0001}$	$58.80^{+1.37}_{-2.04}$	$9.86^{+0.73}_{-0.47}$	$2.60^{+0.01}_{-0.01}$	$5.69^{+0.01}_{-0.01}$	$1672.6^{+8.3}_{-9.3}$	$0.115^{+0.005}_{-0.007}$	$0.017^{+0.002}_{-0.001}$
3	$11{:}21{:}35.1^{+50.9}_{-46.6}$	$57195.4733^{+0.0006}_{-0.0005}$	$87.98^{+0.06}_{-0.07}$	$5.36^{+0.03}_{-0.03}$	$1.28^{+0.03}_{-0.03}$	$1.54^{+0.01}_{-0.01}$	$3909.1^{+95.1}_{-108.3}$	$0.574^{+0.011}_{-0.013}$	$0.066^{+0.002}_{-0.003}$
4	$11{:}28{:}58.2^{+7.5}_{-7.3}$	$57195.4785^{+0.0001}_{-0.0001}$	$68.47^{+1.33}_{-1.42}$	$4.63^{+0.44}_{-0.39}$	$1.58^{+0.02}_{-0.02}$	$2.15^{+0.01}_{-0.01}$	$2050.1^{+8.5}_{-8.3}$	$0.392^{+0.006}_{-0.006}$	$0.032^{+0.003}_{-0.003}$
5[d]	$12{:}30{:}42.6^{+94.2}_{-99.6}$	$57195.5213^{+0.0011}_{-0.0012}$	$75.23^{+0.06}_{-0.05}$	$5.15^{+0.07}_{-0.07}$	$1.72^{+0.01}_{-0.01}$	$2.51^{+0.03}_{-0.03}$	$5496.2^{+186.8}_{-175.8}$	$0.861^{+0.003}_{-0.003}$	$0.148^{+0.003}_{-0.003}$
6	$12{:}32{:}47.6^{+87.4}_{-90.3}$	$57195.5228^{+0.0010}_{-0.0010}$	$85.51^{+0.08}_{-0.08}$	$6.06^{+0.03}_{-0.03}$	$1.71^{+0.01}_{-0.01}$	$2.48^{+0.02}_{-0.02}$	$2404.7^{+73.5}_{-65.0}$	$0.606^{+0.010}_{-0.010}$	$0.081^{+0.002}_{-0.002}$
7	$12{:}39{:}39.5^{+8.8}_{-9.4}$	$57195.5275^{+0.0001}_{-0.0001}$	$87.86^{+0.42}_{-0.28}$	$6.95^{+0.17}_{-0.17}$	$1.20^{+0.05}_{-0.03}$	$1.40^{+0.01}_{-0.01}$	$1756.4^{+11.8}_{-11.9}$	$0.186^{+0.005}_{-0.005}$	$0.023^{+0.001}_{-0.001}$
8	$12{:}42{:}43.2^{+6.6}_{-6.9}$	$57195.5297^{+0.0001}_{-0.0001}$	$87.84^{+0.12}_{-0.20}$	$7.72^{+0.33}_{-0.21}$	$2.10^{+0.01}_{-0.01}$	$3.60^{+0.03}_{-0.04}$	$1491.9^{+13.8}_{-14.6}$	$0.085^{+0.002}_{-0.004}$	$0.012^{+0.001}_{-0.001}$

[a]The emission from the underlying compact jet portion of our model is best fitted by a single power law rather than a broken power law.
[b]The index of the electron energy distribution, p, is not a fitted parameter but rather is solved for using values of τ_0 and equation (4).
[c]The expansion velocity, $\beta_{\rm exp}$, is not a fitted parameter but rather is solved for using values of $\beta_{\rm b}$, i, $\phi_{\rm obs}$ and equation (11).
[d]We note that the receding component for this ejection is not well constrained, as it is modelled primarily by the SMA data at later times when the VLA observations had stopped (see Fig. 6). Therefore, the parameters for this ejection should be treated with caution.

calibration (see the Appendix for details). To do this, we use an iterative process whereby we start with our reference frequency data set, run the MCMC (the walkers are evolved over a series of steps, where the first 500 step 'burn in' period is not retained) until convergence is reached and use the final position of the walkers for the first run as the initial guess for the next run of the MCMC, which will include increasingly more data sets in the fit. To monitor the progress of the MCMC and ensure that correct sampling was occurring, we checked that the acceptance fraction stayed within the suggested bounds (between 0.25 and 0.75). Our criteria for convergence require that the positions of the walkers are no longer significantly evolving. We determine whether this criteria is met by monitoring the chains of each of the walkers through the parameter space, and ensuring that, for each parameter, the intra-chain variance across samples is consistent with the inter-chain variance at a given sample.

Using the multidimensional posterior distribution output from the converged MCMC solution, we create one-dimensional histograms for each parameter. The best-fitting result is taken as the median of these distributions, and the uncertainties are reported as the range between the median and the 15th percentile (−), and the 85th percentile and the median (+), corresponding approximately to 1σ errors. All of the best-fitting parameters and their uncertainties are reported in Table 2. Figs 5 and 6 show the best-fitting model overlaid on our multifrequency light curves. Additionally, with our multidimensional posterior distribution, we can explore the possible two-parameter correlations for our model, where a significant correlation between a pair of parameters can indicate a model degeneracy or a physical relationship between the parameters. In the Appendix section we show correlation plots (Fig. E1), along with the one-dimensional histograms, for pairs of parameters for which we find a correlation, and discuss the significance of such a correlation.

Within the Bayesian formalism, the uncertainties reported in Table 2 are purely statistical, and only represent the credible ranges of the model parameters under the assumption that our model is correct. Given the residuals with respect to the optimal model (Fig. 5 bottom panel), the observations contain physical or observational effects not completely accounted for in our model. To factor in how well our chosen model represents the data, we estimated an additional systematic error for our parameters (displayed in Table D1 of Appendix D). To do this we rerun our MCMC, starting from the best-fitting solution, with an extra variance parameter (effectively modelling all the physical/observational effects not included in our model) in our log probability for each frequency band. This variance is equivalent to the square of the mean absolute deviation of the residuals with respect to our optimal model at each frequency (difference between the best-fitting model and the data). The resulting uncertainties in the parameters after this extra MCMC run will reflect the full (statistical + systematic) uncertainties.

Our broad frequency coverage, in particular the high-sub-mm frequencies, is crucial to the success of our modelling. Detailed substructure detected in the sub-mm bands can be used to separate out emission from different ejections, where their lower frequency counterparts are smoothed out and blended together. As such, modelling the lower frequency emission would not be possible without the critical information the high-frequency sub-mm emission provides and vice versa.

5 DISCUSSION OF THE BEST-FITTING MODEL

Our jet model for V404 Cyg, with a total of eight bi-polar ejection events on top of an underlying compact jet, is able to reproduce the emission in all of our observed frequency bands, matching the flux levels, time lags between frequencies, and the overall morphology remarkably well. With such a large sample of jet ejecta, we can probe the intrinsic ejecta properties, and the distribution of these properties between the different ejection events. In particular, our model characterizes the bulk speeds, peak fluxes, the electron population injected during each event, and the jet geometry, all of which we find can vary between events, with bulk speeds of $0.08 < \beta_{\rm b} < 0.86$ c, peak fluxes of $986 < S_0 < 5496$ mJy, electron energy distribution indices of $1.4 < p < 5.6$ (corresponding to $1.2 < \tau_0 < 2.6$) and observed opening angles of $4.06 < \phi_{\rm obs} < 9.86°$. In the following sections, we discuss these ejecta parameters and what they

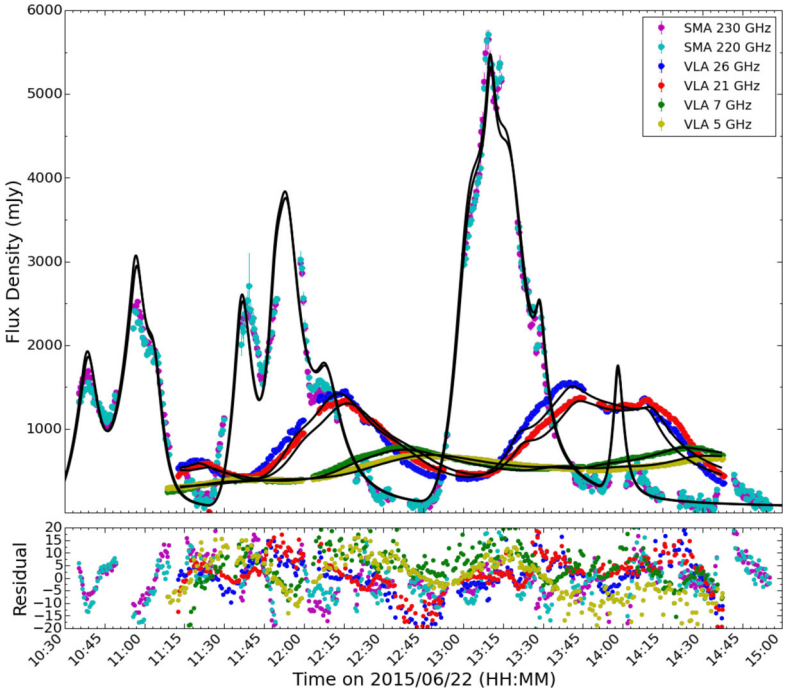

Figure 5. Radio through sub-mm light curves of V404 Cyg on 2015 June 22. In the top panel, we have overlaid the predicted best-fitting model at each frequency (black solid lines) on top of the light curves. The residuals are shown in the bottom panel, where, residual = (data-model)/(observational uncertainties). The JCMT 350 GHz data are not shown in this figure even though they are included in the fit. We do this for the sake of clarity in the figure, due to the small time lag between the JCMT and SMA data (see Fig. 6 for the JCMT 350 GHz light curve and model). With a total of eight bi-polar ejection events, our model can reproduce the emission we observe from V404 Cyg at all of our sampled frequencies remarkably well.

can tell us about jet speeds, energetics, mass loss and geometry. Additionally, we draw comparisons between the V404 Cyg ejection events and the jet oscillation events in GRS 1915+105, as well as other multiwavelength observations of V404 Cyg.

5.1 Jet speeds

The bulk speeds of jet ejecta measured in BHXBs[15] can vary from system to system (e.g. $\Gamma \sim 1$ in SS 433; Hjellming & Johnson 1981, $\Gamma \sim 2$ in V4641 Sgr; Hjellming et al. 2000), where some systems that are known to enter high-luminosity states, like V404 Cyg, have been shown to launch jet ejecta with $\Gamma > 2$ (e.g. GRO J1655−40; Hjellming & Rupen 1995). However, in V404 Cyg we find that the bulk speeds of our modelled ejecta are quite low, with bulk Lorentz factors of only $\Gamma \sim$ 1–1.3 (excluding ejection 5; see footnote c in Table 2 for details).

Moreover, V404 Cyg shows bulk speeds that vary substantially between ejection events, on time-scales as short as minutes to hours. There is some evidence in the literature that jet speeds can vary within a BHXB[16] source. For example, Blundell & Bowler (2005) find small variations in jet speed up to 10 per cent in SS 433, jet speeds have been reported to vary between outbursts of H1743−322 (Corbel et al. 2005; Miller-Jones et al. 2012b), and varying proper motions have been measured in GRS 1915+105 (Miller-Jones et al. 2007). However, no other source has shown variations as large, or on as rapid time-scales as V404 Cyg.

Performing a Monte Carlo Spearman's rank correlation test, we find no correlation between jet speed and ejection time, where, for instance, the bulk speed of the ejections (i.e. $\beta_{\rm b}c$) increased or decreased throughout our observation period. However, we find a potential correlation (Spearman coefficient of 0.83 ± 0.07 with a p-value of 0.01) between bulk speed and peak flux of our modelled ejecta, where brighter ejecta tend to have higher speeds. This correlation is consistent with what was seen in H1743−322, where higher bulk ejecta speeds corresponded to higher radio luminosity measurements (Corbel et al. 2005; Miller-Jones et al. 2012b).

The factors that govern jet speed in BHXBs are not well understood, but our measurements of surprisingly slow speeds, which can vary between sequential jet ejection events, suggest that the properties of the compact object (i.e. black hole mass) or peak luminosity of the outburst are likely not the dominant factors that affect jet speed.

Additionally, given the varying bulk speeds between the ejection events, it is plausible that later, faster ejections could catch up to earlier, slower ejections. Such a collision between ejecta may result in a shock that could be as bright or even brighter than the initial ejections, and in turn produce a flaring profile that could mimic a new ejection event. While including ejecta collisions in our model is beyond the scope of this work, we briefly consider the possibility here by examining the bulk motion of all of the ejections. We find that a collision between ejection 3 and ejection 2 would occur at ∼11:30 (if they were ejected at the same position angle), which is very close to the predicted ejection time of ejection 4. Moreover, ejection 4 has a bulk speed that is in between the

[15] An important caveat when considering the value of the bulk Lorentz factor (Γ), estimated using proper motions of discrete jet ejecta, is that Γ depends strongly on the assumed distance to the source (Fender 2003). While the distance is well known for V404 Cyg, this is not the case for the majority of BHXBs, and as a result constraints on Γ in these systems typically represent lower limits.

[16] There is also evidence of jet speeds varying in neutron star XBs, most notably, Sco X-1 (Fomalont, Geldzahler & Bradshaw 2001a,b) and Cir X-1 (Tudose et al. 2008).

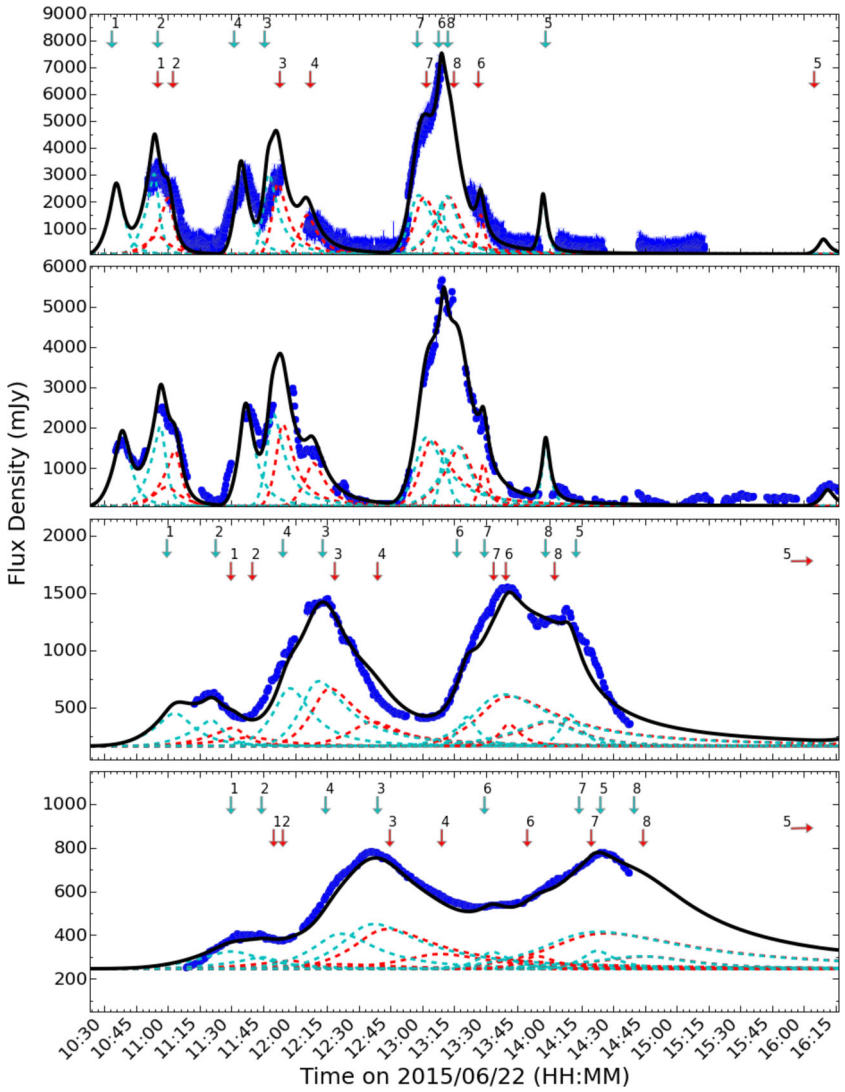

Figure 6. V404 Cyg light curves at representative frequencies; 350 GHz (top), 230 GHz (2nd from top), 26 GHz (third from top) and 7 GHz (bottom). In all panels, the black solid line indicates the total model, and the dotted lines indicate the approaching (cyan) and receding (red) components of the individual ejection events. The arrows (cyan for approaching, red for receding) identify which flares correspond to which ejection number from Table 2. Note that we do not attempt to model all of the sub-mm emission at times after the VLA observations had stopped.

bulk speeds of ejections 2 and 3, as we might expect for the bulk motion of the plasmon after such a collision. However, given that the jet appears to be rapidly precessing in V404 Cyg (Miller-Jones et al. 2017, in preparation), ejections 2 and 3 are launched at very different inclination angles, which would prevent such a collision from occurring. Therefore, given the precessing jet, we find this collision scenario unlikely.

5.2 Jet energetics, mass loss and particle acceleration

In our model, we assumed that the radiating electrons follow a power-law energy distribution. The power-law index of this distribution, p, informs us about the population of accelerated electrons initially injected into each discrete jet component, where the value of this energy index is governed by the electron acceleration mechanism. *Fermi* acceleration by a single shock can produce values of $p \sim 2$–3, which are typically found in XRBs (Bell 1978; Blandford & Eichler 1987; Markoff, Falcke & Fender 2001). However, the energy index can take on a wider range of values under certain conditions, where for example, lower values of p (which result in a more asymmetric flare profile) can be produced if the acceleration occurs in multiple shocks (Melrose & Pope 1993), or if the electrons carry away kinetic power from the shock (Drury & Volk 1981), and higher values of p could be produced in the presence of oblique shocks (although this case requires highly relativistic shocks to produce large p values; Ballard & Heavens 1992). Distributions with values of $p > 4$ are nearly indistinguishable from a thermal (Maxwellian) distribution, which in the shock acceleration paradigm, implies very little acceleration has occurred (a shock essentially takes an input thermal distribution of electrons and builds a power-law distribution up over time). Magnetic reconnection in a relativistic plasma is another viable mechanism that can accelerate electrons into distributions with similar p values to shock acceleration. In this case, smaller p values can be produced in the case of a strongly magnetized plasma ($\sigma > 10$; where $\sigma \equiv B^2/4\pi nmc^2$ represents the magnetization parameter), and larger p values can be produced in a weakly magnetized plasma ($\sigma \sim 1$; Guo et al. 2014; Sironi & Spitkovsky 2014;

Sironi, Giannios & Petropoulou 2016). In either theory of particle acceleration, we would expect a link between the speed (for shock acceleration) or magnetization (for magnetic reconnection), and the energy index, p.

The energy indices of our modelled ejecta appear to vary between sequential ejection events, with $1.4 < p < 5.6$ (where we find no clear correlation between p values and jet speed). These p values could be produced by shock acceleration or magnetic reconnection (under the right conditions), although we would need to invoke different mechanisms to produce distributions in both the very low and very high p regimes (e.g. 1.4 in ejection 7 and 5.7 in ejection 2), which is not entirely physical for a single source. Further, this significant range seen in our energy indices suggests that our model may not be capturing all of the complexities of these ejection events, where the more extreme values of the energy index could be mimicking the effect of physics that has not been included in our model. For instance, the vdL model assumes equipartition, but as the plasmons expand they must do work, which will result in some of the magnetic field dissipating into kinetic or thermal pressure, and in turn, the assumption of equipartition may break down. Simplifications in our model such as this could also explain the lack of expected correlation between our energy indices and the speed of the ejecta. A more rigorous treatment, which, for example, calculates the full synchrotron flux (and does not rely on the equipartition assumption), is beyond the scope of this work, but will be considered in future iterations of this model.

For synchrotron-emitting clouds of plasma injected with our measured electron distributions, we estimate that the minimum energy[17] needed to produce each of our modelled ejection events range from $5.0 \times 10^{35} < E_{\rm min} < 3.5 \times 10^{38}$ erg, with minimum energy magnetic fields[18] of the order of a few Gauss ($1 < B_{\rm min} < 35$ G). Taking into account the duration of each event, these energies correspond to a mean power into each event ranging from $4.0 \times 10^{32} < P_{\rm min} < 2.5 \times 10^{35}$ erg s^{-1}. Due to the slow bulk speeds of the ejecta, including the kinetic energy from the bulk motion [in an electron–positron plasma $E_{\rm KE} = (\Gamma - 1)E_{\rm min}$] yields only slightly higher values of $4.1 \times 10^{32} < P_{\rm tot} < 2.6 \times 10^{35}$ erg s^{-1}. The minimum energy and power released within each of our modelled ejection events is comparatively lower than estimated for other major ejection events in BHXBs ($E_{\rm min} \sim 1 \times 10^{43}$ erg; e.g. Fender et al. 1999b and $P_{\rm tot} \sim 10^{36}$–10^{39} erg s^{-1}; e.g. Fender et al. 1999c; Brocksopp et al. 2007; Curran et al. 2014). This difference is dominated by the difference in the estimated size of the emitting region, where the radii of our modelled ejecta are smaller than is normally estimated for major ejection events, and the low bulk speeds, which result in a much smaller kinetic energy contribution. Considering that the flaring activity in V404 Cyg lasted ∼2 weeks (and assuming our observations to be representative of this entire period), we estimate that the total (minimum) energy (radiative + kinetic) released into jet ejections over the full flaring period is $\sim 3.2 \times 10^{40}$ erg, which is more on par with typical energies estimated for major ejection events in BHXBs. This total energy is also comparable to that carried by the accretion disc wind ($\sim 10^{41}$ erg).[19]

If we assume that the jet ejecta contain some baryonic content, in the form of one cold proton for every electron, we calculate that the mean power into each event (including the kinetic energy from bulk motion) ranges from $6.2 \times 10^{32} < P_{\rm tot} < 3.8 \times 10^{35}$ erg s^{-1}. In this baryonic case, we estimate a total mass lost through the jet in our observation period of 9.4×10^{-13} M$_\odot$ (corresponding to 7.2×10^{-11} M$_\odot$ over the 2 week flaring period). To compare this jet mass loss to the mass accreted on to the black hole, we follow a procedure similar to Munoz-Darias et al. (2016), using simultaneous *INTEGRAL* X-ray observations (only including the harder Integral Soft Gamma Ray Imager bands, ranging from 25 to 200 keV) to calculate the total energy radiated (integrated X-ray luminosity) during our observations. To do this, we convert the count rate into flux in the 10–1000 keV band using a power-law model with photon index $\Gamma_{\rm p} \sim$ 1–2, and approximating the integral as a sum ($\int L_{\rm X}\,{\rm d}t \approx \sum_i L_i \delta t = \bar{L}\Delta T$, where $\bar{L}$ is the weighted mean, δt is size of the time bins and ΔT is the total observation time). Assuming an accretion efficiency of 0.1, we calculate a total mass accreted during our observations of $M_{\rm acc,\,BH} = 3.4 \times 10^{-11}$ to 7.8×10^{-11} M$_\odot$. Therefore, the mass lost in the jet is a small fraction of the total mass accreted, $M_{\rm jet} = (1\text{–}3) \times 10^{-2} M_{\rm acc,\,BH}$, and much less than the mass estimated to be lost in the accretion disc wind ($\sim 1000 M_{\rm acc,\,BH}$; Munoz-Darias et al. 2016).

5.3 Jet geometry and ejecta size scale

Measurements of jet geometry in BHXBs, in particular the observed opening angle, only exist for a handful of systems, where all but one are upper limits (e.g. see table 1 in Miller-Jones et al. 2006, as well as Yang et al. 2010 and Rushton et al. 2017 for recent measurements in XTE J1752−223 and XTE J1908+094). Our simultaneous light-curve modelling technique allows us to directly derive the first measurements of the jet geometry in V404 Cyg, where we model observed jet opening angles of $4.06^\circ < \phi_{\rm obs} < 9.86^\circ$. These measurements are consistent with the opening angle estimates for the other BHXB systems with constraints, where the majority show $\phi_{\rm obs} \lesssim 10^\circ$.

With the opening angles, we can estimate the level of confinement of the jets in V404 Cyg by solving for the intrinsic expansion speed (using Equation 11; see last column of Table 2) of our modelled ejecta ($\beta_{\rm exp} c = \frac{c}{\sqrt{3}}$ indicates freely expanding components, where $\frac{c}{\sqrt{3}}$ represents the speed of sound in a relativistic gas). We find intrinsic expansion speeds of $0.01 < \beta_{\rm exp} < 0.1$ c, indicating a highly confined jet in V404 Cyg. There are many possible mechanisms that could be responsible for confining the jets in V404 Cyg. In particular: the jet could be inertially confined (Icke et al. 1992), where the ram pressure of the strong accretion disc wind detected in V404 Cyg (Munoz-Darias et al. 2016) could inhibit the jet ejecta expansion;[20] the jet could be magnetically confined by a toroidal

[17] In our minimum energy calculations, we perform the full calculations outlined in Longair (2011), where we integrate the electron energy distribution from $\nu_{\rm min} = 150$ MHz to $\nu_{\rm max} = 666$ GHz. The minimum frequency represents the lowest radio detection with LOFAR on June 23 and 24 (Broderick et al. 2015), and the maximum frequency represents our highest frequency sub-mm detection. When we consider an electron–proton plasma, we assume the ratio of the energy in the protons over that of the electrons is $\frac{\epsilon_{\rm p}}{\epsilon_{\rm e}} = 1$.

[18] We note that while these calculations assume equipartition, the system could be far from equipartition. In this case, the magnetic field would not necessarily be equivalent to the minimum energy field, but rather could be either much higher or much lower.

[19] A rough estimate of the energy lost in the accretion disc wind is equivalent to $E_{\rm wind} \sim (1/2) M_{\rm wind} v_{\rm wind}^2$. Using $M_{\rm wind} \sim 10^{-8}$ M$_\odot$ and $v_{\rm wind} \sim 1000$ km s^{-1} (Munoz-Darias et al. 2016), we estimate $E_{\rm wind} \sim 10^{41}$ erg.

[20] Although we note that if the confinement is external, this would suggest that a very large amount of pressure surrounds the ejections. If this is supplied

magnetic field (Eichler 1993); the jet could contain cold protons, which may impede the jet ejecta expansion (Miller-Jones et al. 2006); or a combination of these different mechanisms could be at work.

Further, as we alluded to in the previous section, the initial radii of the jet ejecta (i.e. the radii of the ejecta at the time the sub-mm emission peaks) estimated by our model are noticeably smaller than those typically estimated for major ejection events in other BHXBs. This is likely a result of the much slower expansion velocities ($\beta_{\rm exp} < <1$) we find for the V404 Cyg ejecta. In particular, we infer a range of initial radii for our ejecta ranging from 0.6×10^{12} to 1.3×10^{12} cm. These radii appear to remain similar (to within a factor of 2) between ejection events.

5.4 Underlying compact jet

In addition to the jet ejecta component, we observe an extra constant flux component in our light curves, which varies with frequency. Due to the shape of our estimated spectrum of this emission (see Fig. 2) and the strong compact core jet present throughout the span of our simultaneous VLBA imaging (Miller-Jones et al., in preparation), we interpret this extra flux term as emission from an underlying compact jet. We believe that this compact jet was switched on during the launching of the multiple discrete ejection events. In our best-fitting model, this compact jet emission is characterized by a single power-law spectrum, with an optically thin spectral index of $\alpha = -0.46^{+0.03}_{-0.03}$.

Our suggestion of a compact jet, that has not been fully quenched, is in agreement with the findings of Sanchez-Fernandez et al. (2016), who show that V404 Cyg never fully reached a soft accretion state (where we would likely expect strong quenching of the compact jet; e.g. Rushton et al. 2016), but rather remained in either a harder intermediate or very high state during our observations. Under this interpretation, based on our lowest radio frequency measurement, we place limits on the optically thick to thin jet spectral break frequency of $\nu_{\rm br} < 5.25$ GHz, and flux at the spectral break of $S_{\rm br} > 318$ mJy. However, we note that simultaneous VLA Low Band Ionospheric and Transient Experiment observations (Kassim et al. 2015) detect V404 Cyg at a total time-averaged flux density of 186 ± 6 mJy at 341 MHz. Given that our best-fitting model predicts a maximum jet ejecta flux component of ∼100 mJy at 341 MHz, it is clear that the 341 MHz compact jet component cannot lie along the single power law stated above. As such, the spectral break would therefore occur within the range of $0.341 < \nu_{\rm br} < 5.25$ GHz, which is significantly lower than previous estimates for V404 Cyg made during the hard accretion state ($\nu_{\rm br} = 1.82 \pm 0.27 \times 10^5$ GHz; Russell et al. 2013a,b). This evolution in the location of the spectral break is consistent with the pattern suggested by recent observations (e.g. Corbel et al. 2013; van der Horst et al. 2013; Russell et al. 2014) and MHD simulations (Polko et al. 2014), where, as the mass accretion rate increases during softer accretion states of BHXB outbursts (which usually occur at high luminosities; Koljonen et al. 2015), the jet spectral break moves towards lower radio frequencies prior to the jet switching off (or at least fading below our detection limits).

Up to now we have only considered the compact jet and the ejection events as separate entities. In the presence of explosive, energetic ejection events, we might expect a compact jet to be disrupted. In particular, as the ejecta collide with the pre-existing compact jet, a shock would likely develop, due to the difference in bulk speeds between the two. In this situation, if the compact jet rapidly re-establishes itself after being destroyed by ejecta (before the ejecta propagate far enough away from the black hole to be resolved), we would observe a compact core jet that appears to never shut off. Therefore, we believe it is plausible that a compact jet is being repeatedly destroyed and re-established (on rapid time-scales) following ejection events in V404 Cyg. Further, the emission from such a shock interaction could display an optically thin spectrum (similar to the interaction between the discrete ejecta and the surrounding ISM; e.g. Corbel et al. 2004), like the one we observe for our baseline emission component. Thus, while we interpreted the baseline emission in our light curves as originating only from a compact jet, emission from a possible interaction of the jet ejecta with this compact jet, and/or continuous lower-level, fainter jet ejecta that never get resolved, could also be contributing to the baseline flux level we observe.

Moreover, in our model we have assumed that the compact jet flux component is constant in time. However, as the accretion rate (and in turn the jet power) changes, the flux of a compact jet is expected to change as well (Russell et al. 2014). If we consider the erratic X-ray behaviour observed in the source (which presumably traces a rapidly changing accretion rate), it is plausible that the compact jet component could in fact be variable as well. Exploring the possibility of a variable compact jet component in our model is left for future work.

5.5 Ejecta time lags

Our model predicts that the intrinsic time lag (in the source frame) between a certain frequency (ν) and the reference frequency (ν_0), is represented by,

$$t_{\nu-\nu_0,\rm src} = \left(\frac{R_0}{\beta_{\rm exp}}\right)\left\{\left(\frac{\nu_0}{\nu}\right)^{\frac{p+4}{4p+6}} - 1\right\}, \quad (15)$$

where the observed time lag can be obtained through the transformation, $t_{\nu-\nu_0,\rm obs} = \frac{t_{\nu-\nu_0,\rm src}}{\delta_{\mp}}$.

Fig. 7 shows the observed time lags, predicted by our model, between each frequency band and the ejection time, for the approaching (top panel) and receding (bottom panel) components. The time lags are clearly variable between different ejection events (e.g. ∼10–30 min between the ejection and our reference frequency, 230 GHz), which is a result of the varying ejecta properties (i.e. $\beta_{\rm exp}$, p, R_0).

Further, it is interesting to note that, for a different flaring event that occurred ∼2 d after our data set, Shahbaz et al. (2016) measured a time lag of 2.0 and 3.8 h between the predicted ejection time (indicated by an r'-band polarization flare, which these authors suggest could be the signature of the launching of major jet ejection event) and the flare peaks at 16 and 5 GHz, respectively. These lags are slightly higher than predicted for the approaching components of our modelled ejection events, but appear to share a similar slope across frequencies.

5.6 Comparison to GRS 1915+105

GRS 1915+105 is the only other BHXB in which a similar multifrequency variability pattern to that seen in V404 Cyg has been reported. While flaring activity has been seen in other systems, it

solely by the ram pressure from an accretion disc wind, then the mass-loss rate (proportional to the velocity ratio of the ejections to the wind) would be unrealistically large (i.e. greater than the mass accretion rate).

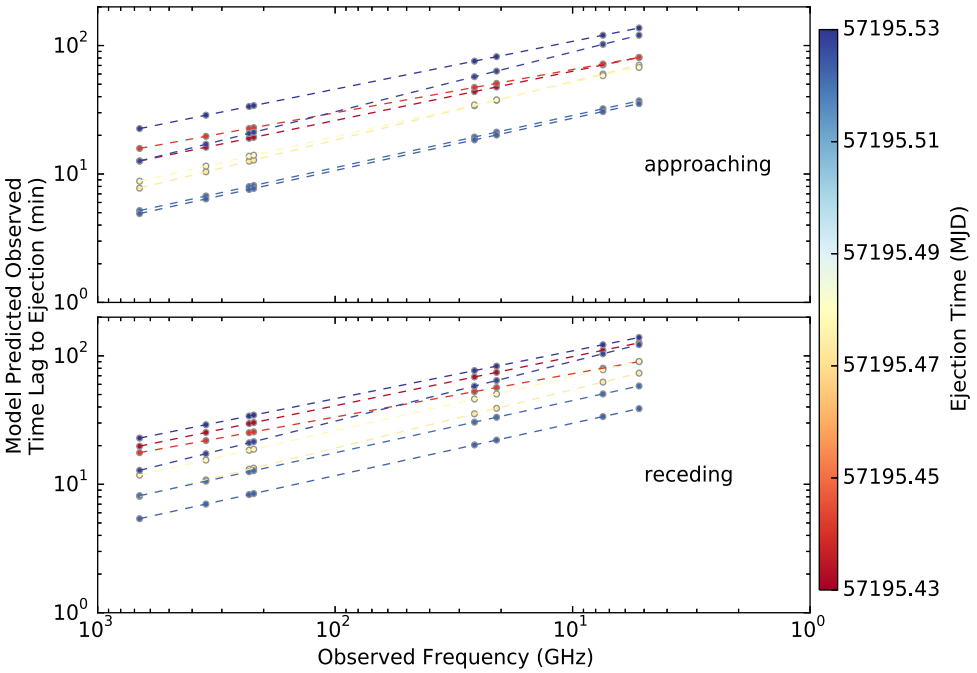

Figure 7. Observed time lag, predicted by our model, between our sampled frequency bands and the time of ejection, for the approaching (top panel) and receding (bottom panel) components of each ejection event. The data points are coloured by ejection time, where the colour bar indicates the ejection time of the event in MJD.

is often only detected in one frequency band (e.g. V4641 Sgr in optical; Uemura et al. 2004), or the flares in question evolved over much longer (days rather than minutes/hours) time-scales (e.g. 4U 1630−47 in radio/X-ray; Hjellming et al. 1999). GRS 1915+105 has displayed some correlated radio, sub-mm and IR flares (with lower frequency emission delayed from higher frequency emission), which repeated every ∼20 min for a ≥10 d period (Fender & Pooley 2000). While no discrete components were resolved with VLBI during the events, the similar rise and decay times of flares at different frequencies suggest that adiabatic energy losses, likely during the expansion of discrete components, played a key role in determining the flaring profiles of these events. In fact, Mirabel et al. (1998) found that the timing of the radio emission during these events was consistent with synchrotron emission from adiabatically expanding plasma clouds, where each event required an energy input of $\sim 10^{39}$ erg, and carried an estimated mass of $\sim 10^{18}$ g. Many studies of these jet ejection events suggest that they occur as a result of instabilities causing the repeated ejection and refilling of the inner accretion disc or coronal flow (e.g. Belloni et al. 1997; Nandi et al. 2001; Vadawale et al. 2001).

In V404 Cyg our modelled ejection times appear to occur on a similar rapid time-scale as seen in GRS 1915+105, where we observe groups of 2–4 ejections (separated by at most ∼20 min), followed by longer periods of up to ∼1 h between groups (see Fig. 8). Each group of ejections seems to correspond to a large flaring event in the light curves. Our estimates of the energetics and mass-loss of the V404 Cyg events (Section 5.2) are also similar to those estimated for the oscillation events in GRS 1915+105, where both are consistent with being smaller scale analogues of major ejection events seen in other BHXBs. Further, Naik et al. (2001) suggested that multiple ejections in GRS 1915+105 could manifest as a single radio flare, similar to the ejection groupings we see in V404 Cyg. However, a noticeable difference in the timing of the V404 Cyg and GRS 1915+105 events is that the V404 Cyg events are not as quasi-periodic (i.e. they do not occur on as regular intervals) when compared to the GRS 1915+105 events, which occurred every ∼20 min (Fender & Pooley 2000). The absence of quasi-periodicity in the V404 Cyg events could indicate that the jet production process is not as stable in V404 Cyg as it was during the GRS 1915+105 events.

The similarity between the morphology, duration and energetics of the rapid ejection periods in V404 Cyg and GRS 1915+105 suggests that the events may have a common origin, possibly in the repeated ejection and refilling of some reservoir in the inner accretion flow. This hypothesis is consistent with the recent finding of Radhika et al. (2016), who report the non-detection of the disc component in the X-ray spectra following major radio flares in V404 Cyg. Although, given the large intrinsic absorption (Motta et al. 2017) seen in V404 Cyg during the outburst, it is conceivable that we may not have been able to detect the soft disc component, even if it was present. Nevertheless, as both V404 Cyg and GRS 1915+105 are long period systems, with large accretion discs, a key ingredient in fuelling rapid, repeated ejection events may be a large accretion disc (as suggested by Kimura et al. 2016; Munoz-Darias et al. 2016).

5.7 Alternative emission models

Other than the vdL model, an alternative emission model that has been used to reproduce flaring light curves in XRBs is the shock-in-jet model (Marscher & Gear 1985; Bjornsson & Aslaksen 2000; Turler, Courvoisier & Paltani 2000). This analytical model, while traditionally favoured for extragalactic sources, has been successfully applied to flaring events in Cyg X–3 (Lindfors et al. 2007; Miller-Jones et al. 2009a), GRO J1655−40 (Stevens et al. 2003) and GRS 1915+105 (Turler et al. 2004). The shock-in-jet model

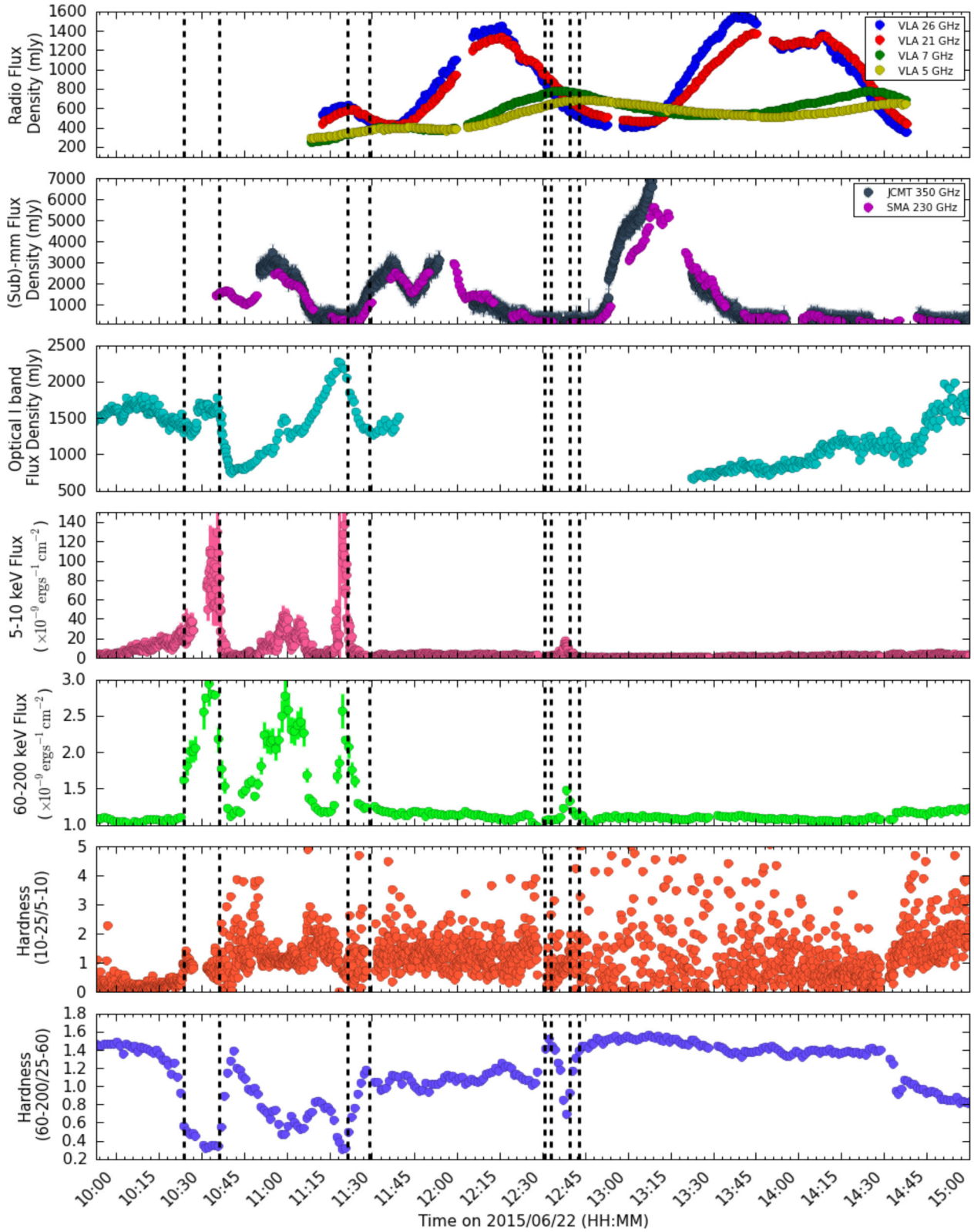

Figure 8. The evolution of the emission properties of V404 Cyg on June 22. Top to bottom the panels represent radio light curves, (sub)-mm light curves, optical light curve (Kimura et al. 2016), soft and hard X-ray light curves, and the 10–15/5–10 keV and 60–100/25–60 keV hardness ratios (Rodriguez et al. 2015). Our modelled ejection times are shown by the dotted vertical lines, where the uncertainties on the ejection times are smaller than the line thickness.

considers a shock wave travelling downstream in a jet flow as the source of each flare in the light curve. Each shock wave will evolve through three different phases; (1) Compton losses dominate, (2) synchrotron losses dominate and (3) adiabatic losses dominate. The main differences between the shock-in-jet model and the vdL model are that the shock-in-jet model considers an initial phase where Compton losses dominate over adiabatic losses, all shock wave events are self-similar, and the electron energy scales differently when compared to the vdL model (shock-in-jet flow expands in 2D, $E \propto R^{-2/3}$; vdL cloud expands in 3D, $E \propto R^{-1}$). These differences will result in a different flare profile between models, where for the same electron population (i.e. same p value), the shock-in-jet model flares will show a much shallower decay, and the peak fluxes at frequencies that are initially optically thin (likely IR and above) will be smaller than predicted by the vdL model (which will overpredict peak fluxes at these frequencies).

As our adapted vdL model is able to reproduce all our light curves (at seven different frequencies) remarkably well, and simultaneous VLBA imaging resolves multiple, discrete components (Miller-Jones et al. 2017, in preparation), we favour the expanding plasmon model over the shock-in-jet model for the V404 Cyg events (although we cannot rule out the shock-in-jet model).

However, for the GRS 1915+105 oscillation events, the emission has been shown to be consistent with both an expanding plasmon model (Mirabel et al. 1998; although we note that these authors only model a single flaring event, and did not include any relativistic/projection effects in their model) and a shock-in-jet model (Turler et al. 2004). If the GRS 1915+105 events are in fact a result of shock waves rather than expanding plasmons, this could explain the notable differences to the V404 Cyg events, namely the quasi-periodicity and the lack of VLBI resolved components.[21] Additionally, as Turler et al. (2004) point out, the shock-in-jet model is still consistent with the scenario that these oscillation events originated with instabilities in the inner accretion disc, as these instabilities could be the catalyst that leads to an increased injection rate of material at the base of the jet, and in turn a downstream shock wave.

5.8 Connection to X-ray and OIR

If the jet ejection events in V404 Cyg are linked to processes occurring in the accretion flow, we might expect our predicted ejection times to correlate well with X-ray/optical and infrared emission. For instance, in GRS 1915+105, IR and radio flares (which are presumably tracers of the ejection events) followed an X-ray peak and occurred during a period of spectral softening (dips in hard X-ray emission). However, the connection is not as clear in V404 Cyg. Fig. 8 displays our predicted ejection times on top of simultaneous X-ray[22] (Rodriguez et al. 2015) and OIR (Kimura et al. 2016) emission.

Flares in the OIR light curve appear to coincide with flares in the X-ray light curves. However, an unfortunate gap in the OIR coverage makes it difficult to confirm that such a pattern holds for the final X-ray flare. In terms of our modelled ejection times, we may be able to tentatively match groups of ejections with specific X-ray/OIR peaks, and possibly local dips in hardness (where the start/end of a steep gradient in hardness appears to correspond to ejections). But it is puzzling that the group that contains the largest number of ejections and produces the largest sub-mm flares appears to be connected to the X-ray flare with the smallest amplitude (although, if an X-ray flare is indicative of a strong dissipative process, more energy dissipated in the X-ray implies less energy would be available to the jets, and vice versa). Further, the second X-ray flare appears to have no jet ejecta counterpart.

Given the extremely high intrinsic absorption during this time period (Motta et al. 2017), it is entirely possible that the flaring in the X-ray light curves is not always dominated by intrinsic source variation, but rather dependent on how much of the inner accretion flow is obscured. This effect was seen in the 1989 outburst, where large changes in column density were determined to be the origin of some of the extreme X-ray variability observed (Oosterbroek et al. 1997; Zycki et al. 1999). Thus, even if the jet ejections are linked to processes in the accretion flow, we may not expect to see a clear correlation between our jet ejections and the X-ray/OIR emission. On the other hand, if the high absorption reduced the X-ray flux artificially, we would expect the high-energy bands (60–200 keV) to be less affected than the lower energy bands (5–10 keV), which does not seem to be the case here. Therefore, the nature of the connection (if any) between our jet ejections and the X-ray/OIR emission is still not fully understood.

5.9 The critical sub-mm perspective

Traditionally XRB jet studies have been dominated by radio frequency observations, such that there only exists a limited set of XRBs that have been observed at mm/sub-mm frequencies (e.g. Paredes et al. 2000; Fender et al. 2001; Russell et al. 2013b; van der Horst et al. 2013; Tetarenko et al. 2015a). When considering time-resolved (<1 d cadence) mm/sub-mm observations, this number decreases to two (i.e. GRS 1915+105; Pooley & Fender 1997, Cygnus X-3; Baars et al. 1986; Fender et al. 1995). However, our work in this paper has clearly shown the vital importance of high time resolution mm/sub-mm data in XRB jet studies. In particular, the mm/sub-mm bands can be used to isolate emission from different flaring events in the light curves, while the lower frequency counterparts of these events tend to be smoothed out and blended together. As such, we find that radio frequency observations alone can often be misleading, especially in terms of identifying and pinpointing the timing of individual rapidly variable flaring events. Including mm/sub-mm monitoring during future XRB outbursts will continue to add key insight to our understanding of jet behaviour.

6 SUMMARY

In this paper, we present the results of our simultaneous radio through sub-mm observations of the BHXB V404 Cyg during its June 2015 outburst, with the VLA, SMA and JCMT. Our comprehensive data set, taken on 2015 June 22 ($\sim$1 week following the initial detection of the outburst), extends across eight different frequency bands (5, 7, 21, 26, 220, 230, 350 and 666 GHz). Using custom procedures developed by our team, we created high time resolution light curves of V404 Cyg in all of our sampled frequency bands. In these light curves, we detect extraordinary multifrequency variability in the form of multiple large amplitude flaring events, reaching Jy level fluxes.

[21] Although, we note that these GRS 1915+105 oscillation events were only observed with multi-element radio-linked interferometer (Fender et al. 1999c), which does not have the resolution to see ejection events of a few mas in size (like those of V404 Cyg).

[22] All X-ray data presented in this paper are taken from the *INTEGRAL* public data products available at http://www.isdc.unige.ch/integral/analysis#QLAsources (Kuulkers 2017, PI: Rodriguez)

Based on the overall morphology, we postulate that our light curves were dominated by emission from a relativistic jet. To understand the source of the emission, we constructed a detailed jet model for V404 Cyg. Our model is capable of reproducing emission from multiple, discrete, bi-polar plasma ejection events, which travel at bulk relativistic speeds (along a jet axis inclined to the line of sight), and evolve according to the van der Laan synchrotron bubble model (van der Laan 1966), on top of an underlying compact jet. Through implementing a Bayesian MCMC technique to simultaneously fit all of our multifrequency light curves with our jet model, we find that a total of eight bi-polar ejection events can reproduce the emission we observe in all of our sampled frequency bands.

Using our best-fitting model to probe the intrinsic properties of the jet ejecta, we draw the following conclusions about the ejection events in V404 Cyg:

(i) The intrinsic properties of the jet ejecta (i.e. speeds, peak fluxes, electron energy distribution indices, opening angles) vary between different ejection events. This results in varying time lags between the flares produced by each ejection at different frequencies.

(ii) The ejecta require (minimum) energies of the order of 10^{35}–10^{38} erg. When taking into account the duration of each event, these energies correspond to a mean power into the ejection events of 10^{32}–10^{35} erg s^{-1}.

(iii) The ejecta carry very little mass ($\sim$1 per cent $M_{\rm acc,\,BH}$), especially when compared to that carried by the other form of outflow detected in V404 Cyg, the accretion disc wind ($\sim$1000 $M_{\rm acc,\,BH}$). However, despite carrying much less mass, we estimate that the ejecta carry similar energy to that of the accretion disc winds.

(iv) We place the first constraints on jet geometry in V404 Cyg, where we find that V404 Cyg contains a highly confined jet, with observed opening angles of the ejecta ranging from 4.06° to 9.86°. While we cannot pin down the main jet confinement mechanism in V404 Cyg, it is possible that the ram pressure of the strong accretion disc wind detected in V404 Cyg (Munoz-Darias et al. 2016) could contribute to inhibiting the jet ejecta expansion, and thus be a key cause of the highly confined jet in this system.

(v) The ejecta travel at reasonably slow bulk speeds, that can vary substantially between events, on time-scales as short as minutes to hours ($\Gamma \sim 1$–1.3).

(vi) Brighter ejections tend to travel at faster bulk speeds.

(vii) Our modelled ejection events appear to occur in groups of 2–4 ejections (separated by at most $\sim$20 min), followed by longer periods of up to $\sim$1 h between groups.

(viii) The rapid time-scale of the ejections is similar to the jet oscillation events observed in GRS 1915+105. Although the V404 Cyg events do not occur on as regular intervals as the GRS 1915+105 events, possibly suggesting the jet production process is not as stable in V404 Cyg.

(ix) We can tentatively match groups of ejections with peaks in simultaneous X-ray/OIR emission. However, the nature of the connection (if any) between our modelled ejection events and X-ray/OIR emission is still not completely clear.

Based on these conclusions, it appears as though the V404 Cyg ejection events are smaller scale analogues of major ejection events, typically seen during the hard to soft accretion state transition in BHXBs. Given the similarity between these rapid ejection events in V404 Cyg and those seen in GRS 1915+105, we postulate that the ejection events in both systems may have a common origin, in the repeated ejection and refilling of some reservoir in the inner accretion flow. This suggests that, in agreement with the findings of Kimura et al. (2016) and Munoz-Darias et al. (2016), the presence of a large accretion disc in both systems may be a key ingredient in producing these rare, rapid ejection events.

Overall, the success of our modelling has shown that, multiple expanding plasmons, on top of a compact jet, is a good match to the emission we observe from V404 Cyg in multiple frequency bands. However, it is also apparent from our results that some simplifications within our model may not fully capture all of the physics of these ejection events (e.g. assuming equipartition, assuming a constant flux from the compact jet), and future iterations of this model will work to address these assumptions and explore their effect on the ejecta properties.

In this work, we have demonstrated that simultaneous multiband photometry of outbursting BHXBs can provide a powerful probe of jet speed, structure, energetics and geometry. Additionally, our analysis has revealed that the mm/sub-mm bands provide a critical new perspective on BHXB jets (especially in the time-domain) that cannot be achieved with radio frequency observations alone. Future high time resolution, multiband observations of more systems, including the mm/sub-mm bands, have the potential to provide invaluable insights into the underlying physics that drives jet behaviour, not only in BHXBs but across the black hole mass and power scale.

ACKNOWLEDGEMENTS

We extend our sincere thanks to all of the National Radio Astronomy Observatory, SMA and JCMT staff involved in the scheduling and execution of these observations. Without their tireless hard work and constant support during this observing campaign, we would never have obtained such an extraordinary data set. We offer a special thanks to Iain Coulson for continuing to share his JCMT expertise. We thank M. Kimura et al. for sharing their OIR data. AJT thanks Eric Koch for many helpful discussions on MCMC implementation and cloud computing, and Patrick Crumley for his helpful comments and feedback on particle acceleration mechanisms. Also, many thanks to Christian Knigge for creating the V404 mailing list and Tom Marsh for creating the V404 observations website. Both of your efforts made it much easier to organize coordinated multifrequency observations of this outburst. AJT is supported by a Natural Sciences and Engineering Research Council of Canada (NSERC) Post-Graduate Doctoral Scholarship (PGSD2-490318-2016). AJT, GRS and EWR are supported by NSERC Discovery Grants. JCAMJ is the recipient of an Australian Research Council Future Fellowship (FT140101082). SM acknowledges support from VICI grant Nr. 639.043.513/520, funded by the Netherlands Organisation for Scientific Research (NWO). TDR acknowledges support from the Netherlands Organisation for Scientific Research (NWO) Veni Fellowship, grant number 639.041.646. Cloud computing time on Amazon Web Services, used for the development and testing of our CASA timing scripts, was provided by the Square Kilometre Array/Amazon Web Services Astro-Compute in the Cloud Program. Additionally, we acknowledge the use of Cybera Rapid Access Cloud Computing Resources, and Compute Canada WestGrid Cloud Services for this work. The National Radio Astronomy Observatory is a facility of the National Science Foundation operated under cooperative agreement by Associated Universities, Inc. The Sub-millimetre Array is a joint project between the Smithsonian Astrophysical Observatory and the Academia Sinica Institute of Astronomy and Astrophysics, and is funded by the Smithsonian Institution and the Academia Sinica. The James Clerk Maxwell Telescope is operated by the East Asian Observatory on behalf of The National Astronomical Observatory of Japan, Academia Sinica Institute of Astronomy and Astrophysics, the Korea Astronomy and Space

Science Institute, the National Astronomical Observatories of China and the Chinese Academy of Sciences (Grant No. XDB09000000), with additional funding support from the Science and Technology Facilities Council of the United Kingdom and participating universities in the United Kingdom and Canada. The authors also wish to recognize and acknowledge the very significant cultural role and reverence that the summit of Mauna Kea has always had within the indigenous Hawaiian community. We are most fortunate to have the opportunity to conduct observations from this mountain.

REFERENCES

Baars J., Altenhoff W., Hein H., Steppe H., 1986, Nature, 324, 39
Ballard K., Heavens A., 1992, MNRAS, 259, 89
Barthelmy S., D'Ai' A., D'Avanzo P., Krimm H., Lien A. Y., Marshall F. E., Maselli A., Siegel M. H., 2015, GCN Circ., 17929, 1
Beardmore A. P., Page K. L., Kuulkers E., 2015, Astron. Telegram, 8455, 1
Bell A., 1978, MNRAS, 182, 147
Belloni T., 2010, in Belloni T., ed., Lecture Notes in Physics, Vol. 794, The Jet Paradigm – From Microquasars to Quasars. Springer-Verlag, Berlin
Belloni T., Mendez M., King A. R., van der Klis M., van Paradijs J., 1997, ApJ, 479, 145
Bernardini F., Russell D. M., Shaw A. W., Lewis F., Charles P. A., Koljonen K. I. I., Lasota J., Casares J., 2016a, ApJ, 818, L5
Bernardini F., Russell D. M., Lewis F., 2016b, Astron. Telegram, 8515, 1
Bjornsson C., Aslaksen T., 2000, ApJ, 533, 787
Blandford R. D., Eichler D., 1987, Phys. Rep., 154
Blandford R. D., Königl A., 1979, ApJ, 232, 34
Blundell K., Bowler M., 2005, ApJ, 622, L129
Brocksopp C. et al., 2002, MNRAS, 331, 765
Brocksopp C., Miller-Jones J. C. A., Fender R. P., Stappers B. W., 2007, MNRAS, 378, 1111
Brocksopp C., Corbel S., Tzioumis A., Broderick J. W., Rodriguez J., Yang J., Fender R. P., Paragi Z., 2013, MNRAS, 432, 931
Broderick J., Stewart A., Fender R., Miller-Jones J., Mooley K., Pietka M., 2015, Astron. Telegram, 7720, 1
Casares J., Charles P. A., 1994, MNRAS, 271, L5
Casares J., Charles P. A., Naylor T., 1992, Nature, 355, 614
Casella P., Pe'er A., 2009, ApJ, 703, L63
Casella P. et al., 2010, MNRAS, 404, L21
Chapin E., Berry D., Gibb A., Jenness T., Scott D., Tilanus R., Economou F., Holland W., 2013, MNRAS, 430, 2545
Collins R., Kaiser C., Cox S., 2003, MNRAS, 338, 331
Corbel S., Fender R., 2002, ApJ, 573, L35
Corbel S. et al., 2001, ApJ, 554, 43
Corbel S., Fender R. P., Tzioumis A. K., Tomsick J. A., Orosz J. A., Miller J. M., Wijnands R., Kaaret P., 2002, Science, 298, 196
Corbel S., Fender R. P., Tomsick J. A., Tzioumis A. K., Tingay S., 2004, ApJ, 617, 1272
Corbel S., Kaaret P., Fender R. P., Tzioumis A. K., Tomsick J. A., Orosz J. A., 2005, ApJ, 632, 504
Corbel S., Kording E., Kaaret P., 2008, MNRAS, 389, 1697
Corbel S., Coriat M., Brocksopp C., Tzioumis A., Fender R., Tomsick J. A. M. M. B., Bailyn C., 2013, MNRAS, 428, 2500
Coriat M. et al., 2011, MNRAS, 414, 677
Curran P. et al., 2014, MNRAS, 437, 3265
Dempsey J. et al., 2012, MNRAS, 430, 2534
Drury L., Volk J., 1981, ApJ, 248, 344
Eichler D., 1993, ApJ, 419, 111
Falcke H., Biermann P., 1995, A&A, 293, 665
Fender R., 2001, MNRAS, 322, 31
Fender R., 2003, MNRAS, 340, 1353
Fender R., 2006, Compact Stellar X-Ray Sources. Cambridge Univ. Press, Cambridge
Fender R., Belloni T., 2004, ARA&A, 42, 317
Fender R. P., Pooley G. G., 1998, MNRAS, 300, 573
Fender R., Pooley G., 2000, MNRAS, 318, L1
Fender R., Bell Burnell S., Garrington S., Spencer R., Pooley G., 1995, MNRAS, 274, 633
Fender R., Garrington S., McKay D., Muxlow T., Pooley G., Spencer R., Stirling A., Waltman E., 1999a, MNRAS, 304, 865
Fender R., Garrington S., McKay D., Muxlow T. W. B., Pooley G., Spencer R., Stirling A., 1999b, MNRAS, 304, 865
Fender R. P., Garrington S. T., McKay D. J., Muxlow T. W. B., Pooley G. G., Spencer R. E., Stirling A. M., Waltman E. B., 1999c, MNRAS, 304, 865
Fender R. et al., 1999d, ApJ, 519, L165
Fender R., Hjellming R., Tilanus R., Pooley G., Deane J., Ogley R., Spencer R., 2001, MNRAS, 322, L23
Fender R., Belloni T., Gallo E., 2004, MNRAS, 355, 1105
Fender R. P., Homan J., Belloni T., 2009, MNRAS, 396, 1370
Ferrigno C. et al., 2015a, Astron. Telegram, 7662, 1
Ferrigno C., Bozzo E., Boissay R., Kuulkers E., Kretschmar P., 2015b, Astron. Telegram, 7731, 1
Fomalont E., Geldzahler B. J., Bradshaw C., 2001a, ApJ, 553, L27
Fomalont E., Geldzahler B. J., Bradshaw C., 2001b, ApJ, 558, 283
Foreman-Mackey D., Hogg D. W., Lang D., Goodman J., 2013, PASP, 125, 306
Gallo E., Fender R., Hynes R., 2005, MNRAS, 356, 1017
Gandhi P., Littlefair S., Hardy L., Dhillon V., Marsh T., Shaw A. W., 2015, Astron. Telegram, 7686, 1
Gazeas K., Vasilopoulos G., Petropoulou M., Sapoutntzis K., 2015, Astron. Telegram, 7650, 1
Goodman J., Weare J., 2010, Comm. App. Math. Comp. Sci., 5, 65
Guo F., Li H., Daughton W., Liu Y., 2014, Phys. Rev. Lett., 113, 15
Han X., Hjellming R. M., 1992, ApJ, 400, 304
Heinz S., Sunyaev R., 2003, MNRAS, 343, L59
Hjellming R. M., Han X., 1995, Radio Properties of X-ray Binaries. Cambridge Univ. Press, Cambridge
Hjellming R. M., Han X.-H., 1989, IAU Circ., 4796, 2
Hjellming R. M., Johnson K., 1981, ApJ, 246, L141
Hjellming R., Johnson K., 1988, ApJ, 328, 600
Hjellming R., Rupen M., 1995, Nature, 375, 464
Hjellming R. M. et al., 1999, ApJ, 514, 383
Hjellming R. M. et al., 2000, ApJ, 544, 977
Holland W. et al., 2013, MNRAS, 430, 2513
Hynes R., Zurita C., Haswell C., 2002, ApJ, 330, 1009
Icke V., Mellema G., Balick B., Eulkerink F., Frank A., 1992, Nature, 355, 524
Kalemci E., Begelman M., Maccarone T. J., Dincer T., Russell T., Bailyn C., Tomsick J., 2016, MNRAS, 463, 615
Kassim N. E. et al., 2015, Astron. Telegram, 7728, 1
Khargharia J., Froning C., Robinson E. L., 2010, ApJ, 716, 1105
Kimura M. et al., 2016, Nature, 529, 54
Kitamoto S., Tsunemi H., Miyamoto S., Yamashita K., Mizobuchi S., 1989, Nature, 342, 518
Koljonen K. et al., 2015, ApJ, 814, 139
Kuulkers E., 2017, Astron. Telegram, 7758, 1
Kuulkers E., Fender R. P., Spencer R., Davis R., Morison I., 1999, MNRAS, 306, 919
Kuulkers E., Motta S., Kajava J., Homan J., Fender R., Jonker P., 2015, Astron. Telegram, 7647, 1
Lindfors E., Turler M., Hannikainen D. C., Pooley G., Tammi J., Trushkin S. A., Valtaoja E., 2007, A&A, 473, 923
Lipunov V. et al., 2015, Astron. Telegram, 8453, 1
Longair M., 2011, High Energy Astrophysics. Cambridge Univ. Press, New York
McMullin J. P., Waters B., Schiebel D., Young W., Golap K., 2007, in Shaw R.A., Hill F., Bell D.J., eds, ASP Conf. Ser. Vol. 376, Astronomical Data Analysis Software and Systems XVI. Astron. Soc. Pac., San Francisco, p. 127
Makino F., 1989, IAU Circ., 4782, 1
Malyshev D., Savchenko V., Ferrigno C., Bozzo E., Kuulkers E., 2015, Astron. Telegram, 8458, 1

Markoff S., Falcke H., Fender R., 2001, A&A, 372, L25
Markoff S., Nowak M., Wilms J., 2005, ApJ, 635, 1203
Marscher A. P., Gear W., 1985, ApJ, 298, 114
Marti-Vidal I., Vlemmings W., Muller S., Casey S., 2014, A&A, 563, 9
Martin-Carrillo A., Murphy D., Hanlon L., Topinka M., van Heerden H. J., van Soelen B., Meintjes P. J., 2015, Astron. Telegram, 7729, 1
Melrose D., Pope M., 1993, Publ. Astron. Soc. Aust., 10, 222
Miller-Jones J. C. A., Fender R., Nakar E., 2006, MNRAS, 367, 1432
Miller-Jones J. C. A., Rupen M. P., Fender R. P., Rushton A., Pooley G. G., Spencer R. E., 2007, MNRAS, 375, 1087
Miller-Jones J. C. A., Rupen M. P., Turler M., Lindfors E., Blundell K., Pooley G. G., 2009a, MNRAS, 394, 309
Miller-Jones J. C. A., Jonker P. G., Dhawan V., Brisken W., Rupen M. P., Nelemans G., Gallo E., 2009b, ApJ, 706, L230
Miller-Jones J. C. A. et al., 2012a, MNRAS, 421, 468
Miller-Jones J. C. A. et al., 2012b, MNRAS, 421, 468
Mirabel I. F., Rodríguez L. F., 1994, Nature, 371, 46
Mirabel I. F., Rodríguez L. F., 1999, ARA&A, 37, 409
Mirabel I. F., Dhawan V., Chaty S., Rodriguez L. F., Marti J., Robinson C. R., Swank J., Geballe T., 1998, A&A, 330, L9
Mooley K., Fender R., Anderson G., Staley T., Kuulkers E., Rumsey C., 2015, Astron. Telegram, 7658, 1
Motta S., Beardmore A., Oates S., Sanna N. P. M. K. A., Kuulkers E., Kajava J., Sanchez-Fernanedz C., 2015a, Astron. Telegram, 7665, 1
Motta S., Beardmore A., Oates S., Sanna N. P. M. K. A., Kuulkers E., Kajava J., Sanchez-Fernanedz C., 2015b, Astron. Telegram, 7666, 1
Motta S. et al., 2016, Astron. Telegram, 8510, 1
Motta S., Kajava J., Sanchez-Fernandez C., Giustini M., Kuulkers E., 2017, MNRAS, 468, 981
Munoz-Darias T., Casares J., Mata Sanchez D., Fender R. P., Armas Padilla M., 2016, Nature, 534, 75
Munoz-Darias T. et al., 2017, MNRAS, 465, L124
Naik S., Agrawal P., Rao A., Paul B., Seetha S., Kasturirangan K., 2001, ApJ, 546, 1075
Nandi A., Chakrabarti S., Vadawale S. V., Rao A. R., 2001, A&A, 380, 245
Negoro H. et al., 2015, Astron. Telegram, 7579, 1
Oates S. R., Motta S., Kuulkers E., Kuin N. P. M., Altamirano D., Gandhi P., Knigge C., Kennea J. A., 2015, Astron. Telegram, 7734, 1
Oosterbroek T. et al., 1997, A&A, 321, 776
Paredes J., Marti J., Peracaula M., Pooley G., Mirabel I., 2000, A&A, 357, 507
Plotkin R., Gallo E., Jonker P., 2013, ApJ, 773, 59
Plotkin R., Gallo E., Markoff S., Homan J., Jonker P., Miller-Jones J., Russell D., Drappeau S., 2015, MNRAS, 446, 4098
Plotkin R. M. et al., 2016, MNRAS, 456, 2707
Plotkin R. M. et al., 2017, ApJ, 834, 19
Polko P., Meier D., Markoff S., 2010, ApJ, 723, 1343
Polko P., Meier D., Markoff S., 2013, MNRAS, 428, 587
Polko P., Meier D., Markoff S., 2014, MNRAS, 438, 559
Pooley G., Fender R., 1997, MNRAS, 292, 925
Primiani R. et al., 2016, J. Astron. Instrum., 5, 19
Radhika D., Nandi A., Agrawal V. K., Mandal S., 2016, MNRAS, 462, 1834
Remillard R., McClintock J., 2006, ARA&A, 44, 49
Richter G., 1989, Inf. Bull. Var. Stars, 3362, 1
Rodriguez J. et al., 2015, A&A, 581, L9
Rushton A. P. et al., 2016, MNRAS, 463, 628
Rushton A. P. et al., 2017, MNRAS, 468, 2788
Russell D. M., Miller-Jones J. C. A., Maccarone T. J., Yang Y. J., Fender R. P., Lewis F., 2011, ApJ, 739, L19
Russell D. et al., 2013a, MNRAS, 429, 815
Russell D. M. et al., 2013b, ApJ, 768, L35
Russell T., Soria R., Miller-Jones J., Curran P., Markoff S., Russell D., Sivakoff G., 2014, MNRAS, 439, 1390
Sanchez-Fernandez C., Kajava J., Motta S., Kuulkers E., 2016, A&A, preprint (arXiv:1608.08802)
Scarpaci J., Maitra D., Hynes R., Markoff S., 2015, Astron. Telegram, 7737, 1
Shahbaz T., Ringwald F. A., Bunn J. C., Naylor T., Charles P. A., Casares J., 1994, MNRAS, 271, L10
Shahbaz T., Russell D., Covino S., Mooley K., Fender R., Rumsey C., 2016, MNRAS, 463, 1822
Sironi L., Spitkovsky A., 2014, ApJ, 783, L21
Sironi L., Giannios D., Petropoulou M., 2016, MNRAS, 462, 48
Sivakoff G. R., Bahramian A., Altamirano D., Miller-Jones J. C. A., Russell D., 2015a, Astron. Telegram, 7763, 1
Sivakoff G. R., Bahramian A., Heinke C., Tetarenko A., Knigge C., Bozzo E., Esposito V., Fender R., 2015b, Astron. Telegram, 7788, 1
Sivakoff G., Bahramian A., Altamirano D., Beardmore A., Kuulkers E., Motta S., 2015c, Astron. Telegram, 7959, 1
Stevens J., Hannikainen D. C., Wu K., Hunstead R., McKay D., 2003, MNRAS, 342, 623
Tanaka Y., Lewin W., 1995, in Lewin W.H.G., van Paradijs J., van den Heuvel E.P.J., eds, X-Ray Binaries. Cambridge Univ. Press, Cambridge, p. 126
Terada K., Miyamoto S., Kitamoto S., Egoshi W., 1994, PASJ, 46, 677
Tetarenko A. J. et al., 2015a, ApJ, 805, 30
Tetarenko A., Sivakoff G., Gurwell M., Petitpas G., Wouterloot J., Miller-Jones J., 2015b, Astron. Telegram, 7661, 1
Tetarenko A., Sivakoff G., Young K., Wouterloot J., Miller-Jones J., 2015c, Astron. Telegram, 7708, 1
Tetarenko A., Sivakoff G. R., Bremer M., Miller-Jones J., Mooley K., Fender R., Staley T., Anderson G., 2015d, Astron. Telegram, 7740, 1
Tetarenko A., Sivakoff G. R., Miller-Jones J., Coulson I., 2016, Astron. Telegram, 8499, 1
Tingay S. J. et al., 1995, Nature, 374, 141
Trushkin S. A., Nizhelskij N. A., Tsybulev P., 2015, Astron. Telegram, 8454, 1
Tsubono K., Aoki T., Asuma K., Daishido T., Kida S., Nakajima H., Niinuma K., Takefuji K., 2015, Astron. Telegram, 7733, 1
Tudose V., Fender R., Tzioumis A. K., Spencer R., van der Klis M., 2008, MNRAS, 390, 447
Turler M., Courvoisier T. J.-L., Paltani S., 2000, A&A, 361, 850
Turler M., Courvoisier T. J.-L., Chaty S., Fuchs Y., 2004, A&A, 415, L35
Uemura M. et al., 2004, PASJ, 56, 61
van der Horst A. et al., 2013, MNRAS, 436, 2625
van der Laan H., 1966, Nature, 5054, 1131
Vadawale S. V., Rao A. R., Nandi A., Chakrabarti S., 2001, A&A, 370, L17
Yang J., Brocksopp C., Corbel S., Paragi Z., Tzioumis T., Fender R., 2010, MNRAS, 409, L64
Yusef-Zadeh F., Wardle M., Heinke C., Dowell C., Roberts D., Baganoff F. K., Cotton W. D., 2008, ApJ, 682, 361
Zurita C., Casares J., Shahbaz T., 2003, ApJ, 582, 369
Zycki P., Done C., Smith D., 1999, MNRAS, 309, 561

SUPPORTING INFORMATION

Supplementary data are available at *MNRAS* online.

Please note: Oxford University Press is not responsible for the content or functionality of any supporting materials supplied by the authors. Any queries (other than missing material) should be directed to the corresponding author for the article.

APPENDIX A: IMAGE WEIGHTING SCHEME

As we are imaging the source on very short time-scales, the uv-coverage in each time bin will be limited. While we do not need to worry about the lack of uv-coverage affecting the fidelity of the images, as the source is point-like at the VLA and SMA resolutions, the side-lobe levels may be a concern. In particular, if the amplitude is changing significantly in each time bin, this implies that we cannot

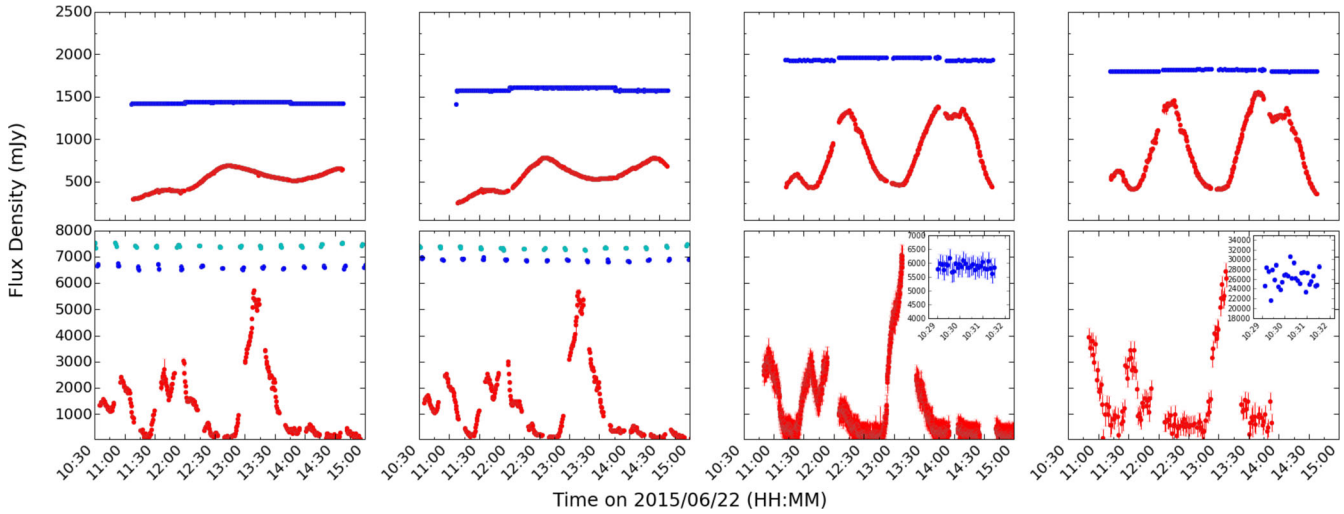

Figure B1. Multifrequency light curves of V404 Cyg and our calibrator sources. *(top)* Left to right the panels represent 5, 7, 21, 26. *(bottom)* Left to right the panels represent 220, 230, 350 and 666 GHz. In all panels, the calibrators are plotted in blue/cyan, while the V404 Cyg data are plotted in red. In the SMA data, the calibrator light curves are scaled up (5000 mJy added to total flux of the two calibrators) for clarity in the plot. In the JCMT data, the calibrator light curves are shown in inset panels as the calibrator scans were taken prior to the target scans.

deconvolve the side-lobes properly. As such, the choice of weighting scheme used while imaging could affect the quality of the images, and in turn the flux density measurements for each time bin. While the side-lobe level is not much of a concern for the VLA, which has reasonably good instantaneous uv-coverage, the SMA is only an eight-element interferometer. In this case, imaging the source with a more uniform weighting scheme minimizes the side-lobe level, and could improve the quality of the images in each time bin. On the other hand, imaging with a natural weighting scheme would maximize sensitivity, leading to lower rms noise levels. After testing different weighting schemes, we find that the choice of weighting had very little effect on the output SMA light curves, where any differences in the flux measurements in each time bin were well within the rms noise. We find that the natural weighting scheme led to lower rms noise and slightly higher dynamic range in the majority of the time bin images. Therefore, we opted to use natural weighting, as the side-lobe level/rms noise trade-off appears to be optimized for natural weighting.

APPENDIX B: CALIBRATOR LIGHT CURVES

Given the large flux variations we detected in our data of V404 Cyg, we wished to check the flux calibration accuracy of all of our observations on short time-scales, and ensure that the variations we observed in V404 Cyg are dominated by intrinsic variations and not atmospheric or instrumental effects. Therefore, we ran our custom procedures to extract high time resolution measurements from our data (see Section 3 for details) on all of our calibrator sources. Fig. B1 displays target and calibrator light curves at all frequencies.

We find that all of our interferometric calibrator sources and our JCMT 350 GHz calibrator display relatively constant fluxes throughout our observations, with any variations (<5 per cent/<10 per cent of the average flux density at radio/(sub)-mm frequencies) being a very small fraction of the variations we see in V404 Cyg. However, our JCMT 666 GHz calibrator scan shows noticeably larger scale variations (∼30 per cent of its average flux level). While these larger variations are not unexpected at this high frequency, as the atmosphere is much more opaque, when combined with the fact that higher noise levels at this frequency prevent us from sampling time-scales shorter than 60 s, we choose to not include the 666 GHz data set in our modelling (although see Appendix B below for a discussion of how well our best-fitting model agrees with the 666 GHz data).

Overall, based on these results, we are confident that the high time resolution light curves of V404 Cyg used in our modelling are an accurate representation of the rapidly changing intrinsic flux of the source.

APPENDIX C: JCMT SCUBA-2 666 GHZ MODEL COMPARISON

While we did not include the JCMT SCUBA-2 666 GHz data in our model fitting, it is still of interest to compare our best-fitting model prediction for the 666 GHz band to the data (see Fig. C1). While our best-fitting model appears to match the timing of the flares in the 666 GHz data quite well, the model tends to overpredict flux in some areas when compared to our data. It is possible that the deviations between the best-fitting model and the data are dominated by the higher flux calibration uncertainty in this band, especially when considering such short time-scales. On the other hand, our model (and the vdL model) are only capable of predicting emission at frequencies that are initially self-absorbed (i.e. optically thick). Thus the deviations between the best-fitting model and the data could also suggest that the emission we observe from the jet ejecta in the 666 GHz band is initially optically thin.

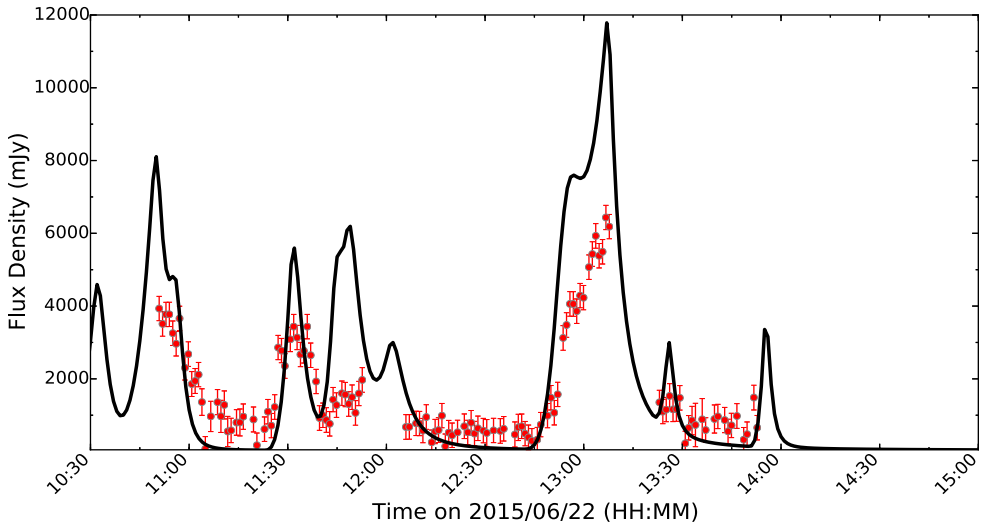

Figure C1. JCMT light curve of V404 Cyg in the 666 GHz band on 2015 June 22. The black solid line represents our predicted best-fitting model in the 666 GHz band.

Table D1. Full (statistical + systematic) errors on V404 Cyg jet model best-fitting parameters.

Compact jet parameters							
$F_{0,\,\mathrm{cj}}$ (mJy)	α						
+3.5, −2.0	+0.05, −0.06						
Individual jet ejecta parameters							
Ejection	t_{ej} (s)	t_{ej} (MJD)	i (°)	ϕ_{obs} (°)	τ_0	F_0 (mJy)	β_{b} (v/c)
1	+25.8, −37.5	+0.0003, −0.0004	+3.01, −6.72	+1.00, −0.34	+0.07, −0.05	+35.4, −40.0	+0.027, −0.047
2	+33.7, −27.3	+0.0004, −0.0003	+1.60, −1.88	+0.43, −0.41	+0.01, −0.01	+45.2, −37.4	+0.011, −0.010
3	+122.7, −98.8	+0.0014, −0.0011	+0.13, −0.14	+0.16, −0.13	+0.03, −0.03	+325.4, −342.5	+0.017, −0.024
4	+28.3, −27.9	+0.0003, −0.0003	+2.45, −3.54	+0.83, −0.51	+0.03, −0.02	+59.5, −87.1	+0.016, −0.019
5	+331.5, −388.6	+0.0038, −0.0045	+0.26, −0.25	+0.35, −0.29	+0.13, −0.11	+389.0, −280.3	+0.013, −0.013
6	+263.8, −378.5	+0.0031, −0.0044	+0.20, −0.18	+0.73, −0.92	+0.14, −0.11	+483.8, −291.9	+0.036, −0.026
7	+27.4, −26.7	+0.0003, −0.0003	+1.22, −0.72	+0.29, −0.23	+0.01, −0.01	+51.1, −51.6	+0.009, −0.010
8	+45.9, −55.5	+0.0005, −0.0006	+0.48, −0.96	+0.62, −0.90	+0.05, −0.05	+85.2, −118.0	+0.007, −0.006

APPENDIX D: SYSTEMATIC ERRORS

As described in Section 4.3, we estimated additional uncertainties on our best-fitting parameters, to factor in how well our chosen model represents the data. Table D1 displays these uncertainties (+for upper confidence interval, − for lower confidence interval) for each fitted parameter.

APPENDIX E: TWO-PARAMETER CORRELATIONS

With the multidimensional posterior distribution output from our MCMC runs, we explored possible two-parameter correlations for our model. A significant correlation between a pair of parameters, that is common to all of the ejecta, could indicate a model degeneracy or a physical relationship between the two parameters. Out of the possible two-parameter pairs, we find interesting correlations involving the i, ϕ_{obs}, F_0 and β_{b} parameters. Fig. E1 displays the correlation plots, along with the one-dimensional histograms of the parameters.[23] The correlation between i and ϕ_{obs} (first column) indicates a known degeneracy in the vdL model. The correlation between F_0 and β_{b} (second column) likely indicates a physical relationship between the parameters, where faster ejecta tend to have brighter fluxes. We find the same relationship when we look at the distribution of bulk speeds and fluxes across all the ejecta, and this relationship has been seen in other sources (see Section 5.1 for details). The final four correlations (columns 3 through 6) seem to indicate a degeneracy between all four parameters (or at least a subset of them), where different combinations of the four parameters could potentially produce similar flaring profiles.

[23] We make use of the CORNER PYTHON module to make these correlation plots; https://github.com/dfm/corner.py

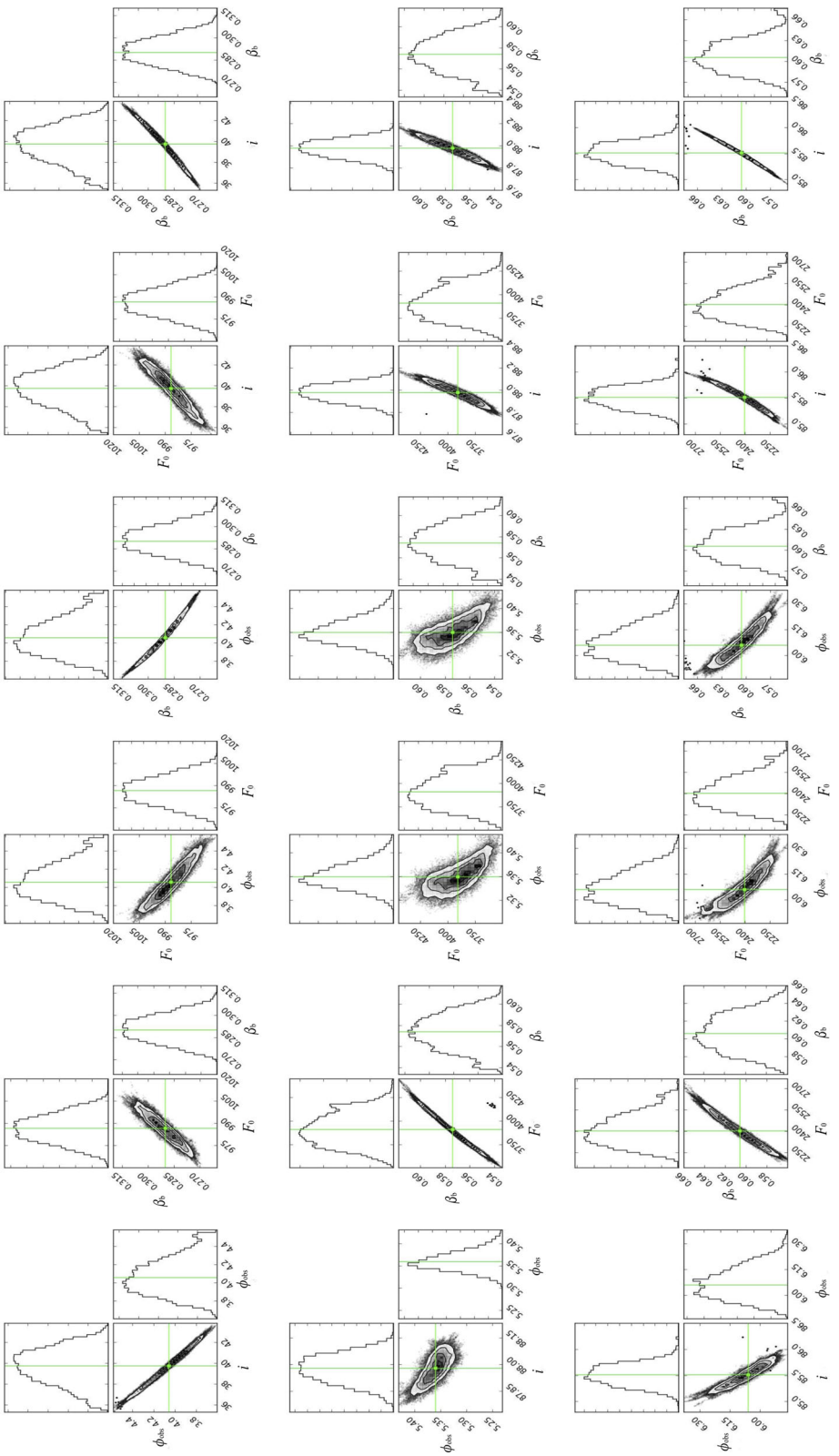

Figure E1. Two-parameter correlation plots for pairs of parameters in our model that show a significant relationship. While all the ejection events display the correlations shown, for clarity we only display the correlation plots for three events, which sample a range of i, $\phi_{\rm obs}$, F_0 and $\beta_{\rm b}$ values, and are spread out in time throughout our observations; ejection 1 (top row), ejection 3 (middle row), ejection 6 (bottom row). The histograms represent the one-dimensional posterior distributions of the parameters, and the green lines/squares indicate the best-fitting value of the parameters.

This paper has been typeset from a TEX/LATEX file prepared by the author.